CANCER

Osteocyte mitochondria inhibit tumor development via STING-dependent antitumor immunity

Hao Zhou[1,2,3]†, Wenkan Zhang[1,2,3]†, Hengyuan Li[2,3,4]†, Fan Xu[5], Eloy Yinwang[1,2,3], Yucheng Xue[1,2,3], Tao Chen[1,2,3], Shengdong Wang[1,2,3], Zenan Wang[1,2,3], Hangxiang Sun[1,2,3], Fangqian Wang[1,2,3], Haochen Mou[1,2,3], Minjun Yao[1,2,3], Xupeng Chai[1,2,3], Jiahao Zhang[1,2,3], Mohamed Diaty Diarra[1,2,3], Binghao Li[2,3,4], Changqing Zhang[6]*, Junjie Gao[6,7]*, Zhaoming Ye[2,3,4]*

Bone is one of the most common sites of tumor metastases. During the last step of bone metastasis, cancer cells colonize and disrupt the bone matrix, which is maintained mainly by osteocytes, the most abundant cells in the bone microenvironment. However, the role of osteocytes in bone metastasis is still unclear. Here, we demonstrated that osteocytes transfer mitochondria to metastatic cancer cells and trigger the cGAS/STING-mediated antitumor response. Blocking the transfer of mitochondria by specifically knocking out mitochondrial Rho GTPase 1 (*Rhot1*) or mitochondrial mitofusin 2 (*Mfn2*) in osteocytes impaired tumor immunogenicity and consequently resulted in the progression of metastatic cancer toward the bone matrix. These findings reveal the protective role of osteocytes against cancer metastasis by transferring mitochondria to cancer cells and potentially offer a valuable therapeutic strategy for preventing bone metastasis.

INTRODUCTION

Bone is a frequent site of cancer metastasis for a wide range of cancers, including lung, breast, and prostate cancers (*1*, *2*). Once cancers metastasize to bone, they are almost incurable and often lead to skeletal morbidity, including bone pain, pathological fractures, nerve compression syndromes, and eventually patient death (*2*). Bone is a highly dynamic organ that hosts a diverse population of cells, including osteoblasts, osteoclasts, and osteocytes (*3*, *4*). Among them, osteocytes are the most abundant cells of bone (>95%) and the major regulators of bone metabolism and homeostasis (*5*, *6*). However, the impact of osteocytes on metastatic cancer cells remains relatively unclear and controversial. Tumor-generated physical forces cause osteocytes to promote the growth of prostate cancer bone metastasis (*7*). Osteocytic connexin 43 hemichannel activity suppresses breast cancer growth and bone metastasis (*8*). A recent study demonstrated that osteocytes and their conditioned medium (CM) can inhibit tumor progression and bone loss by activating Wnt signaling via Lrp5 and β-catenin (*9*).

Osteocytes have a robust network of extensive dendrites that enables direct communication among themselves and with other effector cells in the bone microenvironment (*6*, *10*). Our previous study found that mitochondria were transferred between osteocytes through their dendritic network to maintain the homeostasis of the bone microenvironment (*11*). Beyond the primary role of the "powerhouse" of the cell, mitochondria have been recently viewed as bioenergetic, biosynthesis, and signaling organelles (*12*, *13*). Accumulating evidence has revealed the central role of mitochondria in transducing information not only within cells but also between cells (*13*). Intercellular mitochondrial transfer is a universal biological event that occurs in both physiological and pathological conditions (*14*). Several studies have reported that mitochondria are transferred between tumor cells and other cells to regulate tumorigenesis, therapy resistance, immune invasion, etc. (*15*–*18*). We propose that osteocytes communicate with metastatic cancer cells within the bone microenvironment through their dendritic network by means of intercellular mitochondria transfer.

Here, we used an osteocyte-specific elimination mouse model (DMP1-Cre iDTR) and confirmed a suppressive role of osteocytes on cancer bone metastasis. Next, we identified that osteocytes communicated with cancer cells through mitochondrial transfer using an osteocyte-specific mitochondria reporter mouse model (DMP1-Cre PhAM). This intercellular mitochondrial transfer was mediated by Miro1 and MFN2 and declined with aging (along with the levels of MFN2). Osteocyte-specific deletion of Rho GTPase 1 (*Rhot1*) or mitofusin 2 (*Mfn2*) inhibited intercellular mitochondrial transfer, promoted bone metastasis growth, and decreased immune cell infiltration. Osteocyte mitochondria increased the levels of cytosolic mitochondria DNA (mtDNA) in cancer cells, which activated cGAS-mediated tumor immunogenicity. Collectively, our data indicate that osteocytes have a suppressive effect on cancer bone metastasis by transferring mitochondria to cancer cells, triggering cGAS/STING-mediated antitumor immunity.

RESULTS

Osteocytes play a protective role during bone metastasis

To delineate the role of osteocytes in metastatic cancer progression in vivo, we generated a transgenic mouse model in which osteocytes could be specifically targeted postnatally by diphtheria toxin (DT)–based cell ablation. DMP1-Cre mice were mated with ROSA26-LoxP-DTR (diphtheria toxin receptor) mice to generate DMP1-Cre

[1]Department of Orthopedic Surgery, The Second Affiliated Hospital, Zhejiang University School of Medicine, Hangzhou, Zhejiang, China. [2]Orthopedics Research Institute of Zhejiang University, Hangzhou, Zhejiang, China. [3]Key Laboratory of Motor System Disease Research and Precision Therapy of Zhejiang Province, Hangzhou, Zhejiang, China. [4]Department of Orthopedics, Musculoskeletal Tumor Center, The Second Affiliated Hospital of Zhejiang University School of Medicine, Hangzhou 310009, China. [5]Department of Dermatology, The Second Affiliated Hospital, Zhejiang University School of Medicine, Hangzhou, Zhejiang, China. [6]Department of Orthopedics, Shanghai Sixth People's Hospital Affiliated to Shanghai Jiao Tong University School of Medicine, Shanghai 200233, China. [7]Shanghai Sixth People's Hospital Fujian, No. 16, Luoshan Section, Jinguang Road, Luoshan Street, Jinjiang City, Quanzhou, Fujian, China.
*Corresponding author. Email: yezhaoming@zju.edu.cn (Z.Y.); colingjj@163.com (J.G.); zhangcq@sjtu.edu.cn (C.Z.)
†These authors contributed equally to this work.

iDTR mice (*19*). Dentin matrix protein 1 (DMP1) is highly expressed in osteocytes and odontoblasts but not in osteoblasts (*20*). Administration of DT to DMP1-Cre iDTR mice leads to osteocyte death and causes no short-term impact on trabecular bone mass (*21*). To evaluate the role of osteocytes in metastatic cancer growth, we intratibially injected LLC cancer cells into DMP1-Cre iDTR mutant mice and their littermate control iDTR mice (at day 0) (Fig. 1A). Before cancer implantation, mice were injected with DT to eliminate osteocytes (controls were also injected with DT). As shown in fig. S1 (A and B), the DMP1-Cre iDTR mice had more empty lacunae than the iDTR mice. On day 14, metastatic cancer progression was increased in the osteocyte-eliminated mice compared to the controls (tumor volume, 1545.98 ± 274.65 mm^3 versus 749.78 ± 189.26 mm^3; tumor weight, 1.022 ± 0.262 g versus 0.657 ± 0.143 g; Fig. 1, B and C). Micro-CT (computed tomography) analysis demonstrated decreased trabecular bone volume (BV/TV), trabecular number (Tb.N), and increased trabecular separation (Tb.S) in the Dmp1-Cre iDTR mice compared to the control mice (Fig. 1, D and E). These data suggest a protective role of osteocytes in the bone metastatic microenvironment.

Next, to explore the cellular composition of the bone metastatic microenvironment, we used the CAG-ZsGreen mouse model (*22*). For the same bone metastatic cancer model, LLC cancer cells were injected intratibially into CAG-ZsGreen mice. Fourteen days after cancer cell implantation, the mice were sacrificed, and the tumors were excised and digested. We then isolated infiltrating cells

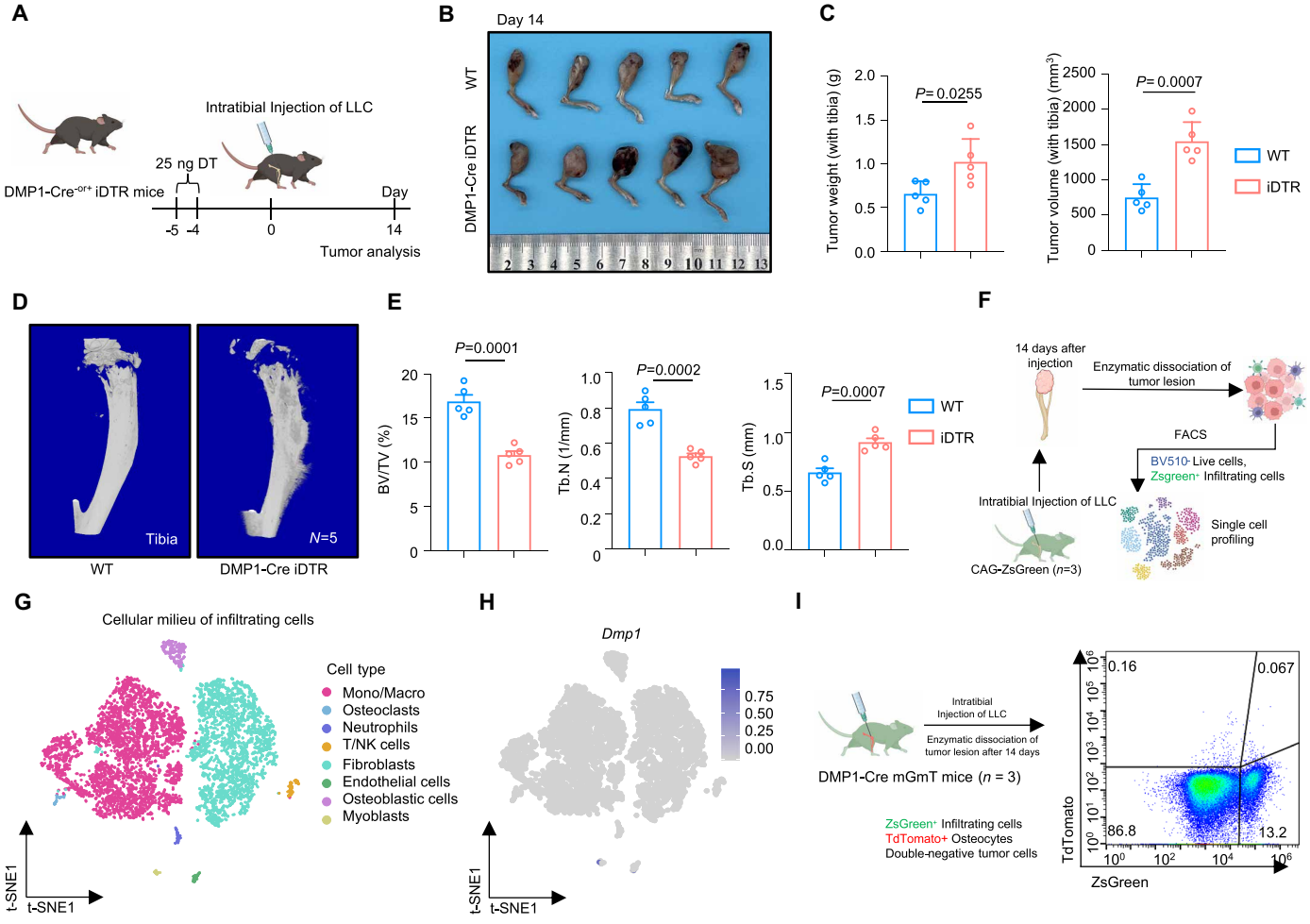

Fig. 1. Osteocytes play a protective role during bone metastasis. (**A**) Experimental design. Ten-week-old DMP1-Cre iDTR and control mice were injected intraperitoneally with 25 ng of DT for two continuous days. Four days later, 1 × 10^6 LLC cells were intratibially injected, and the mice were euthanized after 2 weeks. (**B** and **C**) The intratibial tumor progression increased in DMP1-Cre iDTR mice compared to control mice, as indicated by representative images (B), tumor weight (left), and tumor volume (right) (C) ($N = 5$ for each group). (**D** and **E**) Representative micro-CT images of the tumor-bearing tibia in DMP1-Cre iDTR mice and control mice (D). Micro-CT–based parameters are shown (E): BV/TV, bone volume/total volume (left); Tb.N, trabecular number (middle); Tb.S, trabecular separation (right) ($N = 5$ for each group). (**F**) Experimental design. Eight-week-old CAG-ZsGreen mice were intratibially injected with 1 × 10^6 LLC cells and euthanized after 2 weeks. Tumors were dissected and enzymatically dissociated into single-cell suspensions. Tumor-infiltrating cells ($ZsGreen^+$) were isolated via FACS for scRNA-seq (three tumors from three mice mixed 1:1:1). (**G**) The single cells from isolated tumor-infiltrating cells were clustered into eight major clusters. (**H**) Expression of *Dmp1* in tumor-infiltrating cells. (**I**) Experimental design (left). Eight-week-old DMP1-Cre mG/mT mice were intratibially injected with 1 × 10^6 LLC cells and euthanized after 2 weeks. Tumors were dissected and enzymatically dissociated into single-cell suspensions. Flow cytometry analysis (right) shows the frequency of infiltrating cells ($ZsGreen^+$), osteocytes ($TdTomato^+$), and tumor cells (double negative). Data are presented as means ± SEM. Values were assessed by unpaired two-tailed Student's *t* test in (C) and (E). See also fig. S1.

(ZsGreen$^+$) from the intratibial tumors of the CAG-ZsGreen mice via fluorescence-activated cell sorting (FACS) and used a droplet-mediated single-cell RNA-sequencing (scRNA-seq) platform to profile FACS-purified live tumor-infiltrating cells. We then performed cell classification and marker gene identification using Seurat (STAR methods) (Fig. 1F). We identified and visualized eight major clusters using the T-distributed stochastic neighbor embedding (t-SNE) method based on known cellular markers: monocytes/macrophages, osteoclasts, neutrophils, T/natural killer (NK) cells, fibroblasts, endothelial cells, osteoblastic cells, and myoblasts (Fig. 1G and fig. S1E). In particular, almost no osteocytes (*Dmp1*-expressing cells) (*23*) appeared in the metastatic microenvironment (Fig. 1H). Likewise, the expression levels of other osteocyte signature genes, including *Sost*, *Alpl*, and *Bglap*, were low or absent across the bone metastatic microenvironment (fig. S1F) (*24*). To further investigate the interaction between osteocytes and cancer cells in the bone metastasis microenvironment, we generated DMP1-Cre mGmT reporter mice. Using flow cytometry, we observed similar results, where ZsGreen$^+$ infiltrating cells made up 16.10 ± 4.55% of murine bone metastatic cancer, while no tdTomato$^+$ osteocytes appeared in the tumors (Fig. 1I). The above results indicated that osteocytes cannot infiltrate into tumor spheroids in the bone metastasis microenvironment.

Osteocytes transfer mitochondria to cancer cells during bone metastasis

Next, we sought to probe how osteocytes regulate cancer cells in the bone metastasis microenvironment. Our previous study demonstrated a dendritic network between osteocytes in which mitochondria were shared to maintain bone microenvironment homeostasis (*11*). We then introduced mice with osteocytespecific photoactivatable mitochondria (DMP1-PhAM) to investigate whether osteocytes transfer mitochondria to metastatic cancer cells (*25*). We infected LLC cells with a pLenti-CMV-mCherry-puro lentivirus to construct stable mCherry-expressing LLC cells (LLC-mCherry). LLC-mCherry cells were injected into the tibial or the iliac artery of DMP1-PhAM mice to establish bone metastasis models. After 14 days, tumor-bearing mice were sacrificed, and tumors were isolated for analysis (Fig. 2A). Confocal imaging showed that Dendra2$^+$ mitochondria from osteocytes were present in LLC-mCherry cancer cells in both bone metastasis models (Fig. 2B and fig. S2D), indicating intercellular mitochondrial transfer from osteocytes to metastatic cancer cells. No osteocyte-derived mitochondria were observed in bone marrow (Fig. 2B). Consistently, flow cytometry analysis revealed the presence of dual-positive (mCherry$^+$ and Dendra2$^+$) cells in the tumor (Fig. 2E). Additionally, we sorted and identified cells that received osteocyte-derived mitochondria (Dendra2$^+$) in the tumor based on scRNA-seq analysis (Fig. 2C). Using known cell type–specific gene markers (fig. S2C), we visualized five clusters using the t-SNE method, including LLC-mCherry, macrophages, monocytes, T/NK cells, and fibroblasts. All the clusters that expressed the mCherry sequence were classified as tumor cells, which accounted for 78.52% of osteocyte-derived mitochondria-receiving cells (Fig. 2D).

Several routes of intercellular mitochondrial transfer have been described in recent years, including tunneling nanotubes (TNTs) (*18*, *26*), gap junctions (*27*, *28*), and microvesicles (*29*, *30*). To avoid the possibility of dye leakage from donor cells, we infected the osteocyte cell line MLO-Y4 with pHAGE.mito-dendra2 lentivirus for stable production of mitochondria-specific Dendra2-tagged protein (MLO-Y4-mtDendra2). Confocal imaging demonstrated the colocalization of MLO-Y4–derived Dendra2$^+$ mitochondria within the nanotubes that connected cancer cells and osteocytes (Fig. 2F). After 24 hours of coculture, we observed Dendra2-expressing mitochondria in the cytoplasm of LLC-mCherry cells (Fig. 2G). Confocal sections and orthogonal views also confirmed the presence of Dendra2-expressing mitochondria within LLC-mCherry cells (Fig. 2H). Furthermore, flow cytometry analysis showed that new dual-positive cancer cells (Dendra2$^+$ and mCherry$^+$) appeared after coculture of LLC-mCherry and MLO-Y4-mtDendra2 for 24 hours (Fig. 2I). In addition, we observed that Dendra2-expressing mitochondria from MLO-Y4 cells dynamically migrated toward LLC-mCherry cells (Fig. 2J). Collectively, these data suggest that osteocytes transfer mitochondria to cancer cells via TNT in the bone metastatic microenvironment.

Miro1 and MFN2 regulate mitochondria transfer from osteocytes to cancer cells

Mitochondrial Rho GTPase 1 (Miro1) was reported as a key regulator of TNT-mediated intercellular mitochondrial transfer (*31*, *32*). Furthermore, our previous studies have shown that MFN2 is involved in dynamic mitochondrial movement within the osteocyte dendritic process (*11*). To confirm the role of MFN2 and Miro1 in intercellular mitochondrial transfer between osteocytes and cancer cells, we transfected MLO-Y4-mtDendra2 cells with short hairpin RNA (shRNA) specific for *Mfn2* or *Rhot1* (fig. S3, A to H). We observed that silencing *Mfn2* or *Rhot1* in MLO-Y4-mtDendra2 cells reduced the level of intercellular mitochondrial transfer to LLC-mCherry cells, as determined by flow cytometry after coculture for 24 hours (Fig. 3, A and B, and fig. S3, I and J). Further, a significant increase in mitochondria transfer was observed with overexpression of *Mfn2* or *Rhot1* in MLO-Y4-mtDendra2 cells (Fig. 3, C and D, and fig. S3, K and L).

To investigate the effects of MFN2 or Miro1 on mitochondrial transfer between osteocytes and cancer cells in vivo, we constructed two mouse models with conditional depletion of *Mfn2* or *Rhot1* in osteocytes on the background of DMP1-PhAM mice (*33*). We intratibially injected LLC-mCherry into 8-week-old *Mfn2*$^{-/-}$ DMP1-PhAM, *Rhot1*$^{-/-}$ DMP1-PhAM, and DMP1-PhAM control mice. After 14 days, the mice were sacrificed, and the tumors were excised for further analysis. Confocal imaging demonstrated that the transfer of Dendra2-labeled mitochondria from osteocytes to mCherry-labeled LLC cancer cells significantly decreased after conditional depletion of *Mfn2* or *Rhot1* (Fig. 3, E and F). Consistent with these results, flow cytometry analysis revealed that dual-positive cancer cells decreased significantly after conditional depletion of *Mfn2* or *Rhot1* in osteocytes (Fig. 3, G and H). Together, these findings indicated that MFN2 and Miro1 are implicated in mediating the mitochondrial transfer between osteocytes and cancer cells.

Osteocyte mitochondria inhibit bone metastatic cancer progression

To investigate the effect of osteocyte mitochondria on metastatic cancer cells in vivo, we intratibially injected LLC cancer cells into 8-week-old *Dmp1*^{Cre} *Mfn2*$^{-/-}$ and *Dmp1*^{Cre} *Rhot1*$^{-/-}$ mice and same-age wild-type controls. As shown in Fig. 4A, inhibition of mitochondrial transfer from osteocytes promoted bone metastatic cancer progression compared to the controls (tumor weight, 0.759 ± 0.122 g versus 1.456 ± 0.366 g versus 1.311 ± 0.290 g; tumor

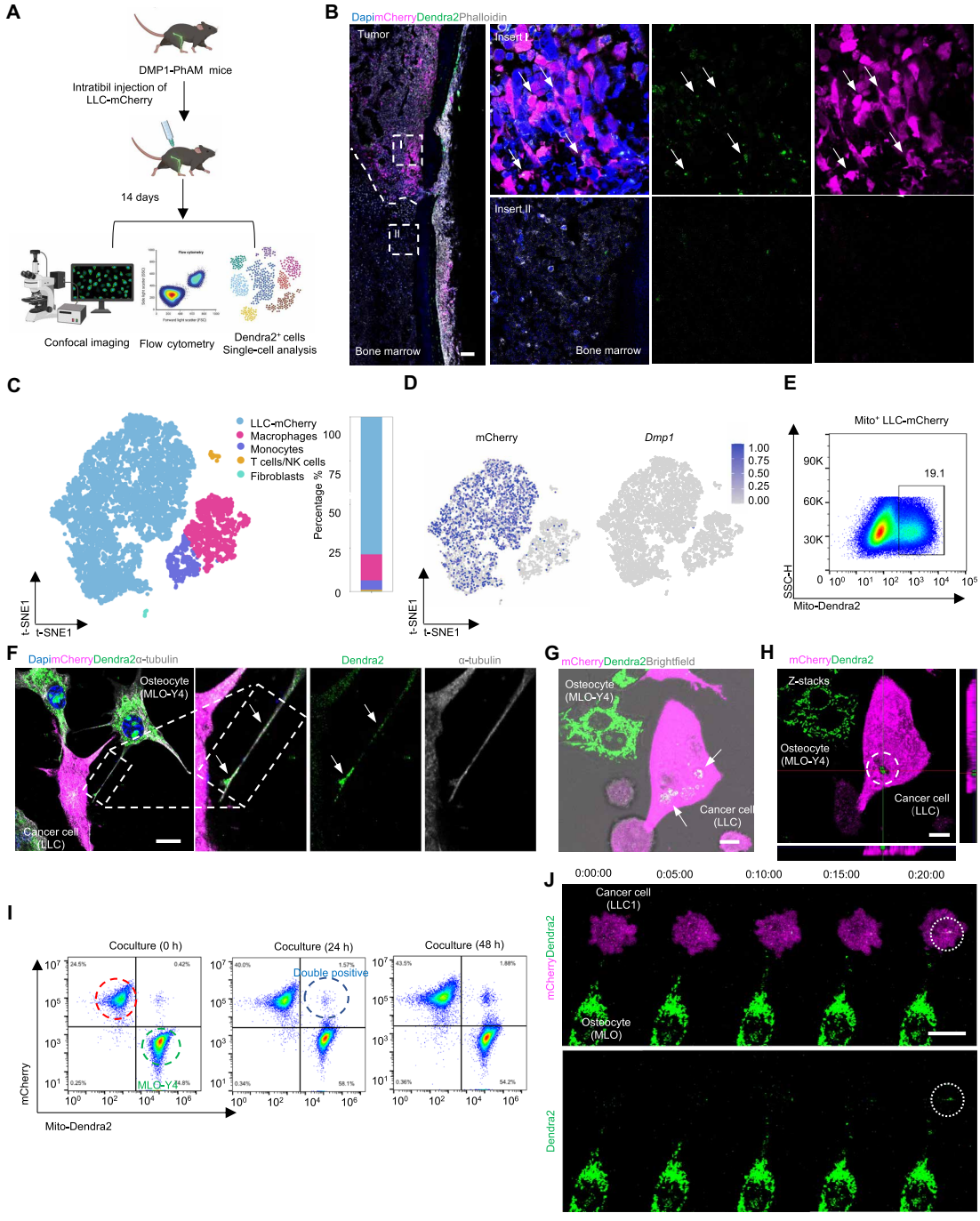

Fig. 2. Osteocytes transfer mitochondria to cancer cells during bone metastasis. (**A**) Experimental design. Eight-week-old DMP1-PhAM mice were intratibially injected with 1×10^6 LLC-mCherry cells and euthanized after 2 weeks. Tumors were dissected for confocal imaging or enzymatically dissociated into single-cell suspensions for flow cytometry analysis, and osteocyte-derived mitochondria recipient cells (Dendra2$^+$) were isolated via FACS for scRNA-seq (three tumors from three mice mixed 1:1:1). (**B**) Confocal image showing osteocyte-derived Dendra2$^+$ mitochondria (arrows) within LLC-mCherry cancer cells (enlarged images in insert I), while no intercellular mitochondrial transfer from osteocytes to bone marrow cells occurred (enlarged images in insert II). Scale bar, 100 μm. (**C**) Single cells from sorted Dendra2$^+$ cells in tumors (three tumors from three mice mixed 1:1:1) were clustered into five major groups (left). The proportion of subpopulations is shown (right). (**D**) Expression of the genes encoding mCherry and *Dmp1*. (**E**) Frequency of LLC-mCherry that received osteocyte-derived Dendra2$^+$ mitochondria. Pregated live LLC-mCherry cancer cells ($N = 3$). (**F**) Representative confocal image showing the presence of Dendra2$^+$ mitochondria (arrows) within a nanotube (α-tubulin positive) between MLO-Y4-meDendra2 cells and LLC-mCherry cells. Scale bar, 10 μm. (**G**) Confocal image showing the transfer of Dendra2$^+$ mitochondria (arrows) in the coculture of MLO-Y4-mtDendra2 cells and LLC-mCherry cells. Scale bar, 10 μm. (**H**) Confocal sections and the corresponding orthogonal views showing the presence of Dendra2$^+$ mitochondria (circle) within LLC-mCherry cells. Scale bar, 10 μm. (**I**) Flow cytometry analysis showing the transfer of Dendra2$^+$ mitochondria from MLO-Y4-meDendra2 cells to LLC-mCherry cells ($N = 3$ for each group). (**J**) Confocal live-cell image showing the dynamic transfer of osteocyte-derived Dendra2$^+$ mitochondria (circle) toward LLC-mCherry cancer cells. Scale bar, 10 μm. See also fig. S2.

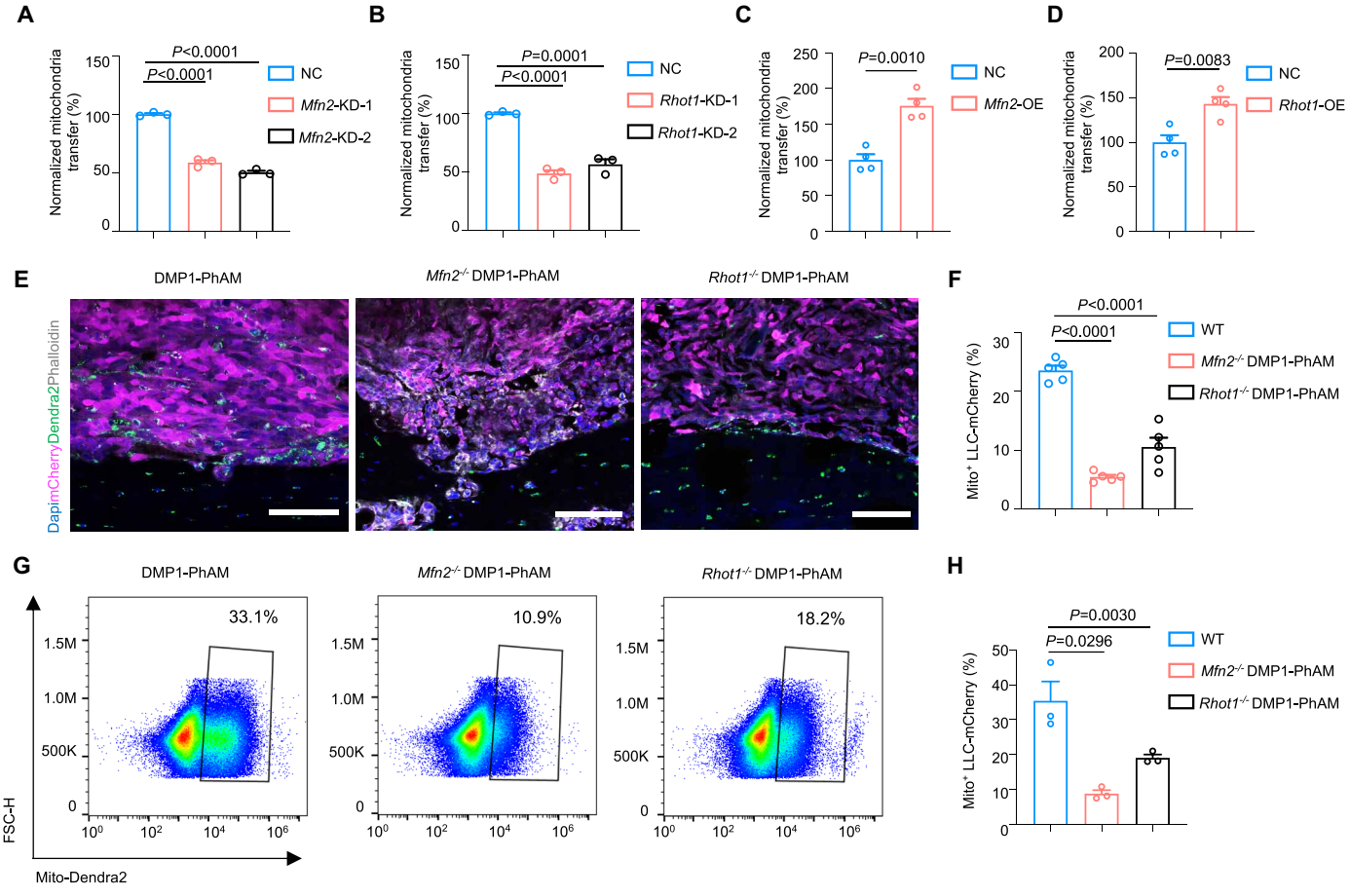

Fig. 3. Miro1 and MFN2 regulate mitochondria transfer from osteocytes to cancer cells. (**A** and **B**) Graphs showing the levels of mitochondrial transfer after shRNA-mediated KD of *Mfn2* or *Rhot1* in MLO-Y4-mtDendra2 cells. Data are normalized to mitochondrial transfer in NC controls ($N = 3$ for each group). (**C** and **D**) Graphs showing the levels of mitochondrial transfer after shRNA-mediated overexpression of *Mfn2* or *Rhot1* in MLO-Y4-mtDendra2 cells. Data are normalized to mitochondrial transfer in NC controls ($N = 4$ for each group). (**E**) Representative confocal images showing the decrease in the transfer of mitochondria in $Mfn2^{-/-}$ DMP1-PhAM mice and $Rhot1^{-/-}$ DMP1-PhAM mice compared to control DMP1-PhAM mice. Scale bar, 100 μm. (**F**) Quantification of cancer cells that received osteocyte-derived mitochondria in confocal images ($N = 5$ for each group). (**G**) Flow cytometry analysis and graphs showing the decrease in the transfer of mitochondria in $Mfn2^{-/-}$ DMP1-PhAM mice and $Rhot1^{-/-}$ DMP1-PhAM mice compared to control DMP1-PhAM mice ($N = 3$ for each group). (**H**) Quantification of cancer cells that received osteocyte-derived mitochondria by flow cytometry ($N = 3$ for each group). Data are presented as means ± SEM. Values were assessed by unpaired two-tailed Student's *t* test in (C) and (D); one-way ANOVA with Dunnett's multiple comparisons test in (A), (B), (F), and (H). See also fig. S3.

volume, 745.34 ± 144.81 mm^3 versus 1947.83 ± 471.17 mm^3 versus 1659.03 ± 189.145 mm^3; Fig. 4B). Micro-CT analysis of the tumor-involved tibia confirmed the presence of osteolytic lesions and demonstrated decreased trabecular bone volume (BV/TV) and trabecular number (Tb.N) after inhibition of mitochondrial transfer compared to the wild-type control (Fig. 4, C and D). We then infected LLC cells with a CMV-mCherry-Luc-blasticidin lentivirus to establish stable luciferase-expressing LLC cells (LLC-mCherry-Luc). LLC-mCherry-Luc cells were injected into the iliac artery of 10-week-old $Dmp1^{Cre}$ $Mfn2^{-/-}$ mice and $Dmp1^{Cre}$ $Rhot1^{-/-}$ mice and same-age wild-type control mice to establish another bone metastasis model. We discovered a similar trend with intra-tibial models that bone metastasis progression was increased in $Dmp1^{Cre}$ $Mfn2^{-/-}$ mice and $Dmp1^{Cre}$ $Rhot1^{-/-}$ mice compared to control wild-type mice as indicated by in vivo bioluminescence imaging (Fig. 4, E and F).

Previous studies reported that cancer cells with deficient mitochondrial DNA acquire mitochondria from the host stroma resulting in partial recovery of their mitochondrial function and a higher proliferative status (*34*, *35*). We thus investigated the level of mitochondrial respiration after mitochondria transfer in the context of bone metastasis, and we observed that cancer cells isolated from $Dmp1^{Cre}$ $Mfn2^{-/-}$ mice and $Dmp1^{Cre}$ $Rhot1^{-/-}$ mice (with suppressed mitochondrial transfer) had a higher level of mitochondrial respiration compared to those isolated from wild-type mice (fig. S4, A and B).

Apart from that, the levels of MFN2 in cortical bone protein declined along with age, as was shown by immunoblotting (Fig. 4G). We also observed a decrease in the expression of mitochondrial trafficking–related genes (including *Mfn2* and *Rhot1*) in the cortical bone of aged (18-month-old) mice compared to young (1-month-old) mice (Fig. 4H). As shown in fig. S5 (A and B), osteocyte numbers in murine cortical bone decreased with age. We then intratibially implanted LLC-mCherry into young (2-month-old), mature (6-month-old), and aged (18-month-old) DMP1-PhAM mice. Confocal imaging of metastatic tumors showed a consistent

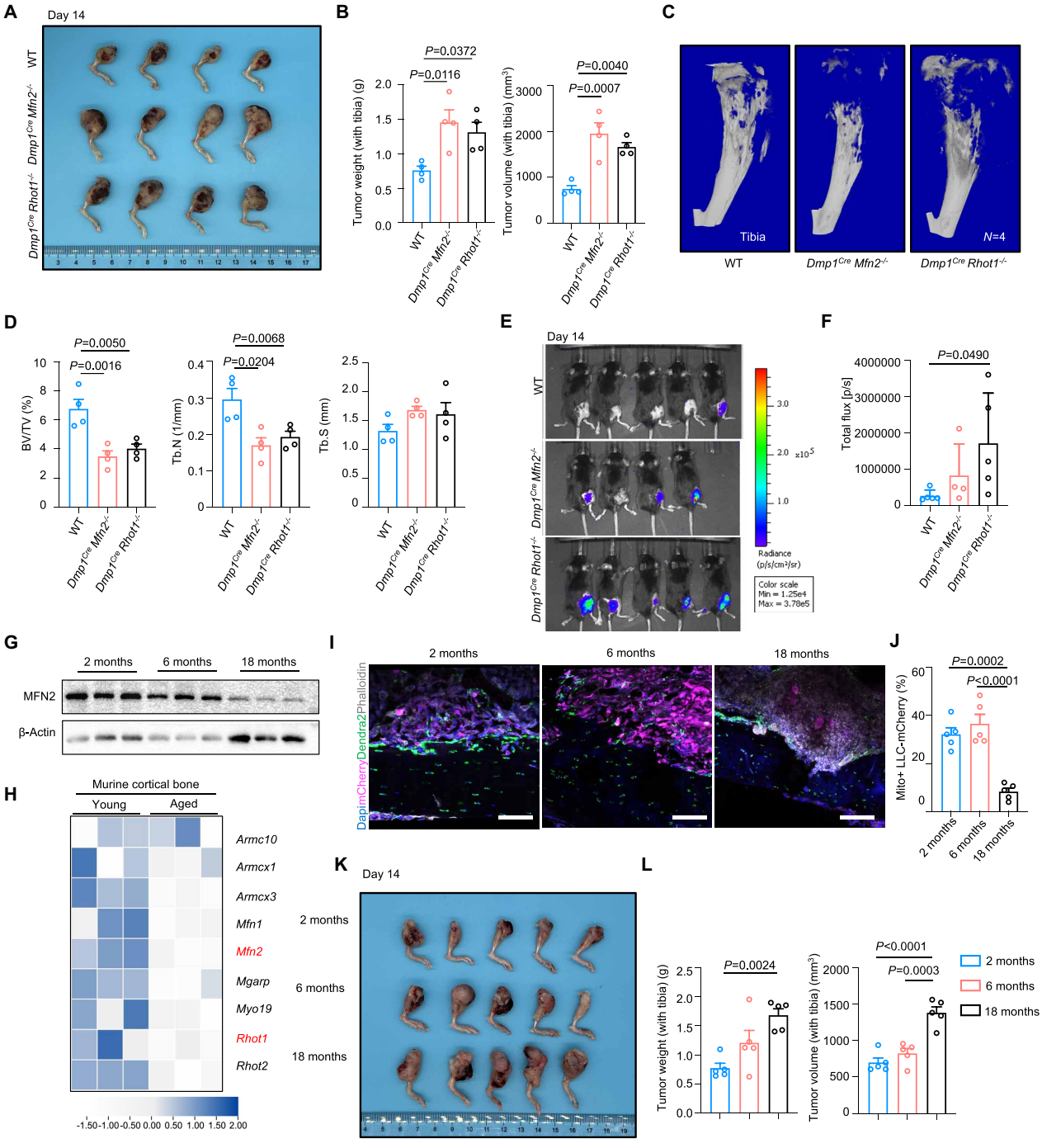

Fig. 4. Osteocyte mitochondria inhibit bone metastatic cancer progression. (**A** and **B**) Intratibial tumor progression was increased in *Dmp1*^{Cre} *Mfn2*$^{-/-}$ mice and *Dmp1*^{Cre} *Rhot1*$^{-/-}$ mice compared to control wild-type mice, as indicated by representative images (A), tumor weight (left), and tumor volume (right) (B) ($N = 4$ for each group). (**C** and **D**) Representative micro-CT images of the tumor-bearing tibia in *Dmp1*^{Cre} *Mfn2*$^{-/-}$ mice, *Dmp1*^{Cre} *Rhot1*$^{-/-}$ mice, and control wild-type mice (C). Micro-CT–based parameters are shown (D): BV/TV, bone volume/total volume; Tb.N, trabecular number; Tb.S, trabecular separation ($N = 4$ for each group). (**E** and **F**) In vivo bioluminescence imaging showed that bone metastasis progression was increased in *Dmp1*^{Cre} *Mfn2*$^{-/-}$ mice and *Dmp1*^{Cre} *Rhot1*$^{-/-}$ mice compared to control wild-type mice ($N = 4$ to 5 for each group). (**G**) Protein levels of MFN2 in cortical bone from young (2-month-old), mature (6-month-old), and aged (18-month-old) mice ($N = 3$ for each group). (**H**) Heatmap showing differential expression of mitochondrial trafficking–related genes in cortical bones from young (1-month-old) and aged (18-month-old) mice ($N = 3$ for each group). (**I**) Representative confocal images showing the decrease in the transfer of mitochondria in aged (18-month-old) DMP1-PhAM mice compared to mature (6-month-old) and young (2-month-old) DMP1-PhAM mice. Scale bar, 100 μm. (**J**) Quantification of cancer cells that received osteocyte-derived mitochondria in confocal images in young (2-month-old), mature (6-month-old), and aged (18-month-old) mice ($N = 5$ for each group). (**K** and **L**) The intratibial tumor progression increased in aged (18-month-old) mice compared to mature (6-month-old) and young (2-month-old) mice, as indicated by representative images (K), tumor weight (left), and tumor volume (right) (L) ($N = 5$ for each group). Data are presented as means ± SEM. Values were assessed by one-way ANOVA with Dunnett's multiple comparisons test. See also figs. S4 and S5.

decline in intercellular mitochondrial transfer from osteocytes to cancer cells with age in DMP1-PhAM mice (Fig. 4, I and J). Additionally, we demonstrated that intratibial tumor progression increased in the aged (18-month-old) mice compared to the mature (6-month-old) and young (2-month-old) mice (tumor weight, 1.681 ± 0.110 g versus 1.208 ± 0.213 g versus 0.775 ± 0.083 g; tumor volume, 1379.75 ± 80.62 mm^3 versus 824.93 ± 65.86 mm^3 versus 698.90 ± 61.64 mm^3; Fig. 4, K and L). Our data revealed that osteocyte mitochondria transfer to cancer cells inhibits bone metastatic cancer progression in the bone microenvironment. The levels of intercellular mitochondrial transfer decrease with age, which may contribute to the progression of bone metastatic cancer in the bone microenvironment.

Osteocyte mitochondria increase cytosolic mtDNA in cancer cells and activate STING pathway via cGAS

Mitochondrial DNA (mtDNA) is a potent damage-associated molecular pattern (DAMP) that has been reported to activate the cGAS/STING innate immune pathway (*36*). To test whether exogenous mitochondria transfer into recipient cells and activate the cGAS/STING pathway, we applied MitoCeption to artificially and quantitatively transfer mitochondria into cancer cells (*37*). As shown in fig. S6A, we validated the effective transfer of $Dendra2^+$ mitochondria isolated from MLO-Y4-mtDendra2 to LLC-mCherry by MitoCeption using flow cytometry. Confocal imaging also showed the uptake of osteocyte-derived mitochondria by LLC cells (fig. S6, B and C).

We transplanted osteocyte mitochondria into LLC cells and performed subcellular fractionation after 24 hours. The efficient subcellular fractionation was validated by staining for lamin A/C, TOM20, voltage-dependent anion selective channel (VDAC), and glyceraldehyde-3-phosphate dehydrogenase (GAPDH) (fig. S6D). The relative levels of cytosolic mtDNA were measured by quantifying DNA containing specific mitochondrial (16*S* rRNA, mt-Nd1, and mt-ATP6) and nuclear (18*S* rRNA) genes in cytosolic and nuclear fractions by quantitative polymerase chain reaction (qPCR). We found a significant increase in the cytosolic mtDNA of mitochondria in the mitochondria-transplanted group compared to the control group (Fig. 5A). Confocal imaging also showed that the double-stranded DNA (dsDNA) signal in the cytosol outside of mitochondria was more prominent in the cells that received osteocyte mitochondria (Fig. 5B). Transplantation of osteocyte mitochondria into LLC cells resulted in the activation of cGAS/STING, as shown by significantly higher levels of pSTING (S365), pTBK1 (S172), pIRF3 (S396), and downstream nuclear factor κB (NF-κB) pP65 (S536) (Fig. 5C). Concomitantly, the expression of STING-dependent proinflammatory genes (*Il1b*, *Il6*, *Ccl4*, *Ifnb*, and *Ifit1*) was significantly up-regulated after mitochondrial transfer by MitoCeption (Fig. 5D). The observed activation of the STING pathway by osteocyte mitochondria was abrogated by knockdown (KD) of *Cgas* in cancer cells (Fig. 5, C and D). Furthermore, we isolated cancer cells from intra-iliac artery model of $Dmp1^{Cre}$ $Mfn2^{-/-}$ mice, $Dmp1^{Cre}$ $Rhot1^{-/-}$ mice, and wild-type control mice and detected a similar trend of significantly up-regulated expression of STING-dependent proinflammatory genes (*Il1b*, *Il6*, *Ccl4*, *Ifnb*, and *Ifit1*) in wild-type mice (Fig. 5E). These results demonstrated that osteocyte mitochondria could activate cGAS/STING pathway in cancer cells. To confirm the activation of cGAS/STING by cytosolic mtDNA, we transfected LLC cells with mtDNA isolated from MLO-Y4 cells. STING-dependent proinflammatory genes (*Il1b*, *Il6*, *Ccl4*, *Ifnb*, and *Ifit1*) were up-regulated after mtDNA transfection (fig. S6G).

On the basis of previous reports, BAX plays a critical role in regulating the release of mtDNA from mitochondria (*38*, *39*). We thus isolated mitochondria from *Bax* KD MLO-Y4 cells and transferred them into LLC cancer cells. We found that mitochondria from *Bax* KD MLO-Y4 cells cannot increase the levels of cytosol mtDNA cancer cells (Fig. 5F). In addition, we found a significantly increased mtDNA level in the mitochondria fraction of LLC cells that receive mitochondria from *Bax* KD MLO-Y4 cells (Fig. 5G). These results suggested that the release of mtDNA from osteocyte mitochondria to the cytosol of cancer cells is dependent on BAX.

Osteocyte mitochondria improve tumor immunogenicity and induce antitumor immunity

Recent studies have reported that the activation of cGAS/STING in cancer cells results in the production of the dinucleotide cGAMP, which triggers the activation of the STING pathway in dendritic cells (DCs) and macrophages, which in turn induces $CD8^+$ T and NK protective antitumor immunity (*40*, *41*). Next, we sought to probe the change in the immune microenvironment after the inhibition of intercellular mitochondrial transfer. To comprehensively understand the change in immune microenvironment composition, we isolated tumors from tumor-bearing $Dmp1^{Cre}$ $Mfn2^{-/-}$ mice, $Dmp1^{Cre}$ $Rhot1^{-/-}$ mice, and wild-type controls and then performed scRNA-seq. After sorting out $CD45^+$ (*Ptptrc*-expressing) immune cells, we identified and visualized eight major clusters based on known cellular markers using the t-SNE method: T cells, B cells, NK cells, neutrophils, DCs, monocytes, macrophages, and $Ctsk^+$ cells (Fig. 6, A and B, and fig. S8D). We observed an increase in the proportion of T cells. Consistently, we detected a significant decrease in tumor-infiltrating immune cells, including $CD4^+$ T cells, $CD8^+$ T cells, and cytotoxic granzyme B^+ $CD8^+$ T cells, in $Dmp1^{Cre}$ $Mfn2^{-/-}$ mice and $Dmp1^{Cre}$ $Rhot1^{-/-}$ mice (Fig. 6, C and E to G). Next, a 9-plex bead-based assay was performed to quantify the levels of inflammatory mediators within the bone metastasis microenvironment. Several critical inflammatory cytokines, including interleukin-1α (IL-1α), IL-1β, and IL-18, growth factors, and chemokines, decreased after inhibition of intercellular mitochondrial transfer in vivo (Fig. 6I), indicative of less potent immune activation within the bone metastasis microenvironment. According to classical markers, we reclustered myeloid cells into 12 subgroups, including a majority of the cells identified as monocytes/macrophages (80 to 90%) and a minority (<20%) identified as DCs (Fig. 6J and fig. S8E). Compared to the wild-type control group, the DC subgroup from both the $Dmp1^{Cre}$ $Mfn2^{-/-}$ and $Dmp1^{Cre}$ $Rhot1^{-/-}$ groups showed a decline in total proportion, including conventional type 1 DCs (cDC1), conventional type 2 DCs (cDC2), migratory DCs (mDCs), and plasmacytoid DCs (pDCs) (Fig. 6, K and L). Consistently, we observed a decrease in total tumor-infiltrating DCs ($CD45^+MHC\text{-}2^+CD11c^+$) using flow cytometry analysis (Fig. 6, D and H). DCs are a group of specialized antigen-presenting cells that stimulate lymphocytes to initiate antitumor responses within the tumor microenvironment (*42*). To further monitor the activation status of these tumor-infiltrating DCs, we found that a series of DC maturation markers (*Cd40*, *Cd83*, *Cd80*, *Cd86*, and *Rebl*) were down-regulated in cDC1s in both the $Dmp1^{Cre}$ $Mfn2^{-/-}$ and $Dmp1^{Cre}$ $Rhot1^{-/-}$ groups (Fig. 6M). Collectively, these data indicated that the inhibition of intercellular mitochondrial transfer from osteocytes to cancer cells promoted bone metastatic cancer progression and decreased immune infiltration, turning "hot" tumors into "cold" tumors.

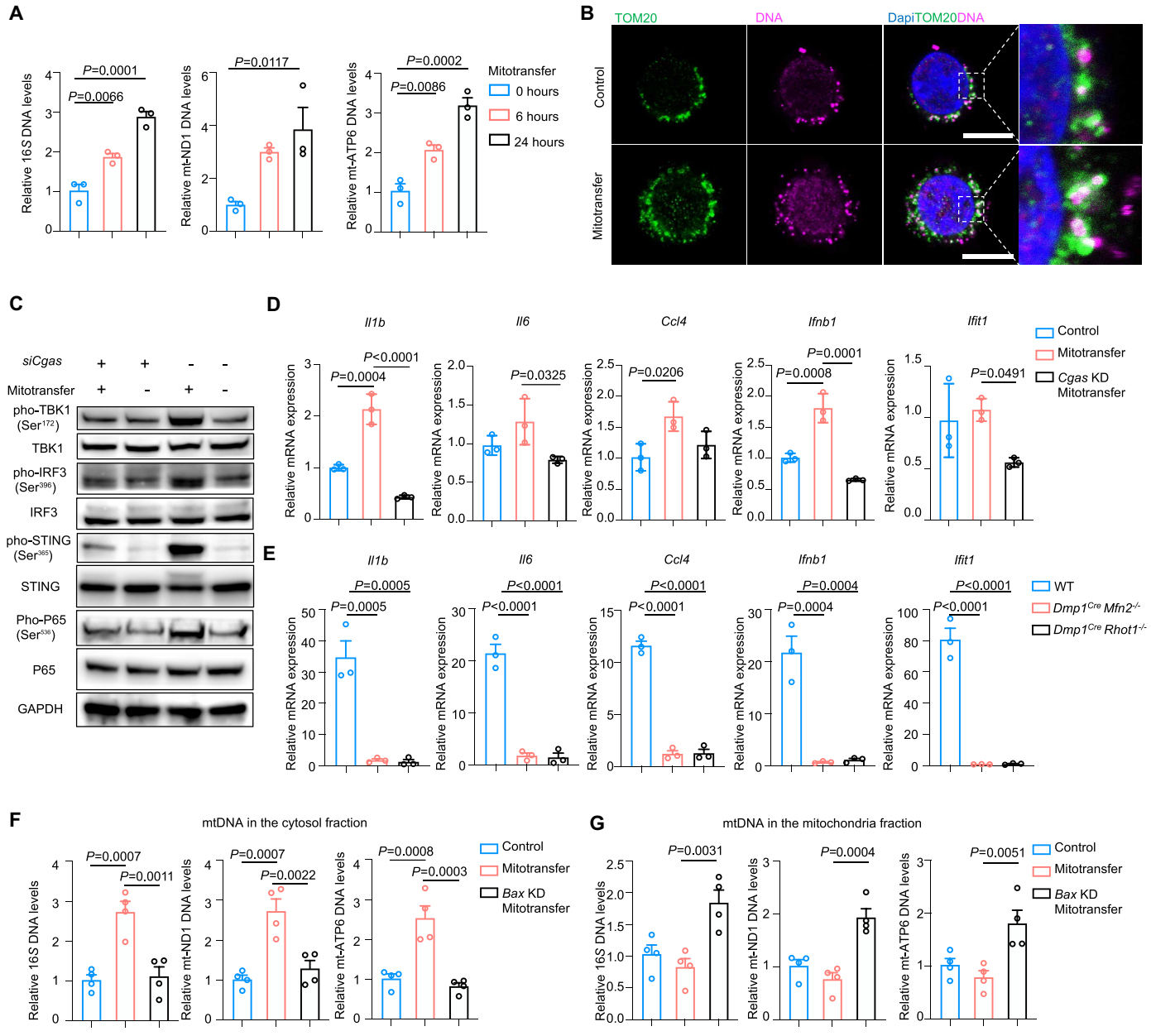

Fig. 5. Osteocyte mitochondria increase cytosolic mtDNA in cancer cells and activate STING via cGAS. (**A**) Relative levels of cytosolic mtDNA (16*S*, mt-Nd1, and mt-ATP6) after transfer of MLO-Y4–isolated mitochondria into LLC cells. Data were normalized to the nuclear 18*S* DNA levels. Data are representative of four independent experiments. (**B**) Representative confocal images of LLC cells stained with anti-DNA, anti-TOM20 antibodies, and DAPI after transfer of MLO-Y4–isolated mitochondria. Scale bar, 10 μm. (**C**) Protein levels of the cGAS/STING pathway after transfer of MLO-Y4–isolated mitochondria into LLC or *Cgas* KD LLC cells. (**D**) Relative mRNA expression of STING-dependent inflammatory cytokines after transfer of MLO-Y4–isolated mitochondria into LLC or *Cgas* KD LLC cells. Data are representative of three independent experiments. (**E**) Relative mRNA expression of STING-dependent proinflammatory genes in LLC cells isolated from intra-iliac artery model of $Dmp1^{Cre}\,Mfn2^{-/-}$ mice, $Dmp1^{Cre}\,Rhot1^{-/-}$ mice, and wild-type control mice. Data are representative of three independent experiments. (**F**) Relative levels of cytosolic mtDNA (16*S*, mt-Nd1, and mt-ATP6) after transfer of mitochondria isolated from control MLO-Y4 or *Bax* KD MLO-Y4 cells into LLC cells. Data are representative of four independent experiments. (**G**) Relative levels of mtDNA (16*S*, mt-Nd1, and mt-ATP6) in the mitochondria fraction after transfer of mitochondria isolated from control MLO-Y4 or *Bax* KD MLO-Y4 cells into LLC cells. Data are representative of four independent experiments. Data are presented as means ± SEM. Values were assessed by one-way ANOVA with Dunnett's multiple comparisons test. See also fig. S6.

DISCUSSION

Our study reveals a previously unknown mechanism by which osteocyte mitochondria inhibit tumor development in the bone marrow microenvironment. We show that osteocytes transfer mitochondria to cancer cells and activate STING pathway by increasing cytosolic mtDNA levels. Further, inhibition of intercellular mitochondrial transfer between osteocytes and cancer cells promotes metastatic cancer progression and decreases immune infiltration (Fig. 7). This work provides evidence of a way of intercellular communication between osteocytes and cancer cells. Osteocytes are multifunctional signaling cells that maintain bone homeostasis by integrating and transmitting hormonal and mechanical signals (*6*). Previous

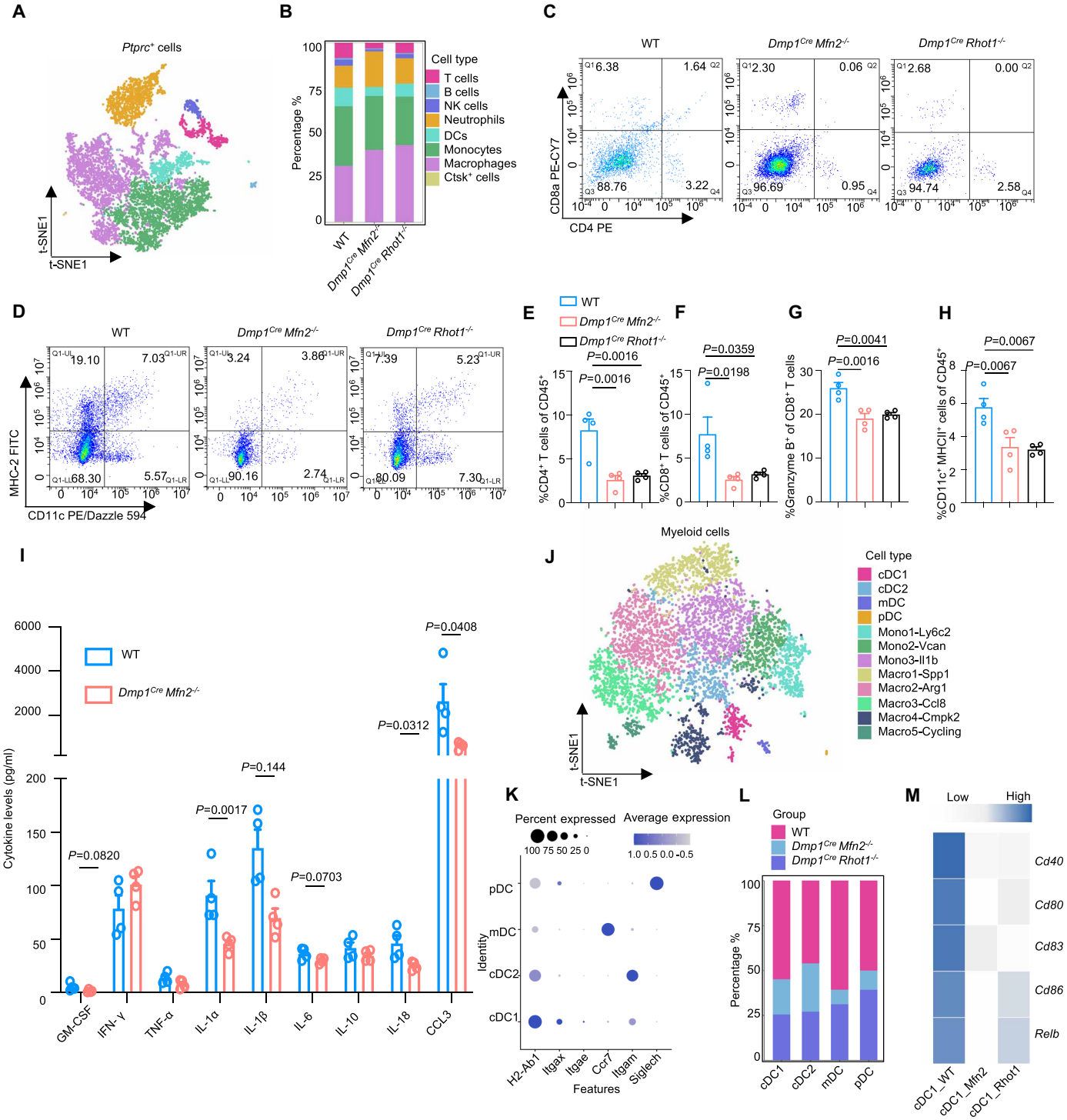

Fig. 6. Osteocyte mitochondria improve tumor immunogenicity and induce antitumor immunity. (**A**) Immune cells (*Ptprc*$^+$) were reclustered into eight clusters according to classical markers. (**B**) Proportion of immune cell subpopulations in *Dmp1*^{Cre} *Mfn2*$^{-/-}$ mice, *Dmp1*^{Cre} *Rhot1*$^{-/-}$ mice, and control wild-type mice (three tumors from three mice mixed 1:1:1 for each group). (**C** to **H**) Flow cytometry analysis and graphs showing a significant decrease in immune cell infiltration within the tumor tissues in *Dmp1*^{Cre} *Mfn2*$^{-/-}$ mice and *Dmp1*^{Cre} *Rhot1*$^{-/-}$ mice compared to control wild-type mice [(C) and (D)], including CD4$^+$ T cells (E), CD8$^+$ T cells (F), cytotoxic granzyme B$^+$ CD8$^+$ T cells (G), and CD11c$^+$ MHCII$^+$ DC cells (H) ($N = 4$ for each group). (**I**) Multiplex analysis of intratumoral cytokines in *Dmp1*^{Cre} *Mfn2*$^{-/-}$ mice and control wild-type mice ($N = 4$ for each group). (**J** and **K**) Myeloid cells were reclustered into 12 clusters according to classical markers. (**L**) Proportion of DC subpopulations derived from *Dmp1*^{Cre} *Mfn2*$^{-/-}$ mice, *Dmp1*^{Cre} *Rhot1*$^{-/-}$ mice, and control wild-type mice (three tumors from three mice mixed 1:1:1 for each group). (**M**) DC maturation–related gene expression in DC subpopulations. Data are presented as means ± SEM. Values were assessed by one-way ANOVA with Dunnett's multiple comparisons test. See also figs. S7 and S8.

studies demonstrated that osteocytes regulate cancer cells by endocrine or paracrine mechanisms. For example, osteocytes release adenosine triphosphate (ATP) via Cx43 hemichannels to inhibit breast cancer cell migration and tumor development (*43*). Conditional medium from osteocytes inhibits tumor progression and osteolysis through Wnt signaling (*9*). Direct communication between osteocytes and cancer cells has also been reported. In multiple myeloma, cell-to-cell contact activates bidirectional Notch signaling in osteocytes and MM cells (*44*). We concluded that during the colonization stage of bone metastasis, osteocytes form contacts with cancer cells and initiate intercellular mitochondrial transfer as a means of cell communication. The mitochondrion is the most complex and multifunctional organelle within eukaryotic cells, and the exchanges of such organelle directly modulate cellular status in recipient cells including oxidative phosphorylation (OXPHOS) functions, reactive oxygen species (ROS), and mtDNA copy number (*45*). Here, our study makes a leap in the understanding and proposes that osteocytes produce output signals that regulate the surrounding cancer cells in the bone metastasis microenvironment through the transfer of whole mitochondria, which also links to the perspective that mitochondria function as signaling hubs at cellular and organismal levels (*13*, *46*). Thus, our data suggest a more direct and efficient way of regulation in osteocytes. However, the relative contribution of different kinds of temporal and spatial intercellular communication by osteocytes in the bone microenvironment remains to be determined.

We confirmed the overall anticancer role of osteocytes in bone metastasis through the genetic elimination of endogenous osteocytes. It is known that osteocytes are one of the most important coordinators among cells in the bone microenvironment, especially osteoclasts and osteoblasts (*47*, *48*). The imbalance of osteoclast-mediated osteolysis and osteoblast-mediated bone formation leads to bone destruction in bone metastasis (*2*, *3*). Although the driver we used, DMP1-Cre, is restricted only to osteocytes and odontoblasts (*20*), we cannot rule out the possibility that the change of bone marrow circumstance due to the elimination of osteocytes may have an impact on bone metastatic cancer progression.

In this study, we investigate mitochondrial transfer in the bone microenvironment based on lung cancer model, as lung is one of the most common origin sites of bone metastasis (*49*). Lung cancer is the leading cause of cancer death worldwide (*50*); 40% of lung cancer cases develop bone metastasis eventually. Lung cancer typically

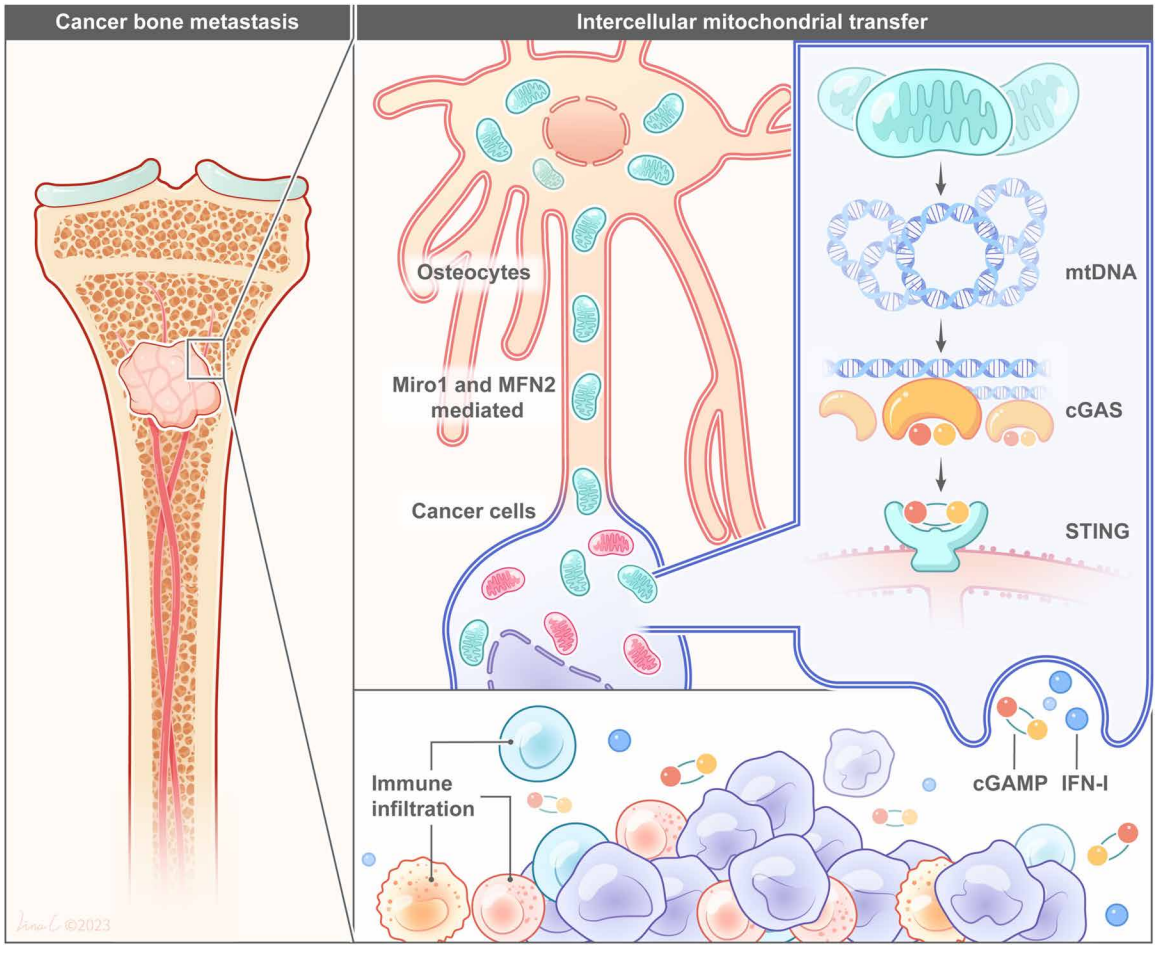

Fig. 7. Schematic representation of the model by which osteocyte mitochondria are transferred into cancer cells, inducing antitumor immunity via cGAS/STING. In our proposed model, osteocyte mitochondria were transferred into cancer cells via nanotubes. Miro1- and MFN2-mediated intercellular mitochondrial transfer increases mtDNA levels in the cytosol of cancer cells and activates the cGAS/STING pathway, enhancing tumor immunogenicity and inducing antitumor immunity.

forms osteolytic bone metastasis and shares some common pathophysiological mechanisms of metastases with breast cancer and multiple myeloma (*2*). In addition, intercellular mitochondria transfer has been implied in other cancer cells including breast cancer (*18*) and melanoma cells (*51*, *52*). Therefore, it is worth our attention if intercellular mitochondrial transfer from osteocytes to cancer cells is a universal phenomenon across cancer types in the bone microenvironment.

The mechanisms underlying intercellular mitochondrial transfer are still largely unknown. Our data discovered that osteocyte mitochondria are transferred to cancer cells via TNTs, which are mediated by Miro1 and MFN2. Many studies have demonstrated the essential role of Miro1 in mitochondrial exchange by tethering mitochondria to cytoskeletal motor proteins and regulating the transport of organelles (*53*). MFN1/2 have been found to interact with the TRAK/Miro complex (*54*) and could be one of the possible proteins anchoring mitochondria to tubulin (*55*). Our previous study showed that MFN2 tethers mitochondria to the endoplasmic reticulum (ER) and mediates mitochondrial transfer within the osteocytic dendritic network (*11*). The underlying mechanisms of how MFN2 interacts with Miro proteins in facilitating mitochondrial transfer are worth investigating for future therapeutic targets. Further research will also be needed to determine if there are other routes of intercellular mitochondrial transfer between osteocytes and cancer cells including extracellular vesicles (EVs), gap junctions, or the internalization of mitochondria.

The generation of *Dmp1*^{Cre} *Mfn2*$^{-/-}$ mice and *Dmp1*^{Cre} *Rhot1*$^{-/-}$ mice allowed us to investigate the effects of osteocyte-derived mitochondria on metastatic cancer cells. Inhibition of intercellular mitochondrial transfer promotes metastatic cancer growth and increases bone destruction, indicating the protective role of osteocyte mitochondria. Previous studies reported that mitochondria-deficient or damaged cancer cells can acquire intact mitochondria with their mtDNA to restore OXPHOS functions, resulting in the recovery of their proliferative status (*34*, *35*, *52*). Other studies mentioned that cancer cells injured by chemotherapy increased mitochondria transfer from other cells as a way to recover their mitochondrial functions (*16*, *56*). These are important works that broaden the understanding of cancer cell biological behavior and the function of mitochondria transfer in cancer. On the other hand, in this study, we focused on the intercellular mitochondria transfer from osteocytes to metastatic cancer cells with functional mitochondria. We also discovered notable decreases in OXPHOS functions and energy metabolism in LLC cells after the transfer of osteocyte mitochondria in the context of bone metastasis. The next question that we will investigate is whether the anticancer role of mitochondria is specific to the bone microenvironment.

Next, we revealed that intercellular mitochondrial transfer increases mtDNA levels in recipient cancer cells and triggers cGAS/STING antitumor response. mtDNA is a potent DAMP that can stimulate the innate immune system by multiple routes, including cGAS, Toll-like receptor 9 (TLR9), and the NLRP9 inflammasome (*57*). Multiple studies have reported that mtDNA-containing EVs can activate the cGAS/STING cytosolic DNA–sensing pathway in recipient cells (*58*–*60*). Recent data have expanded the role of cGAS/STING in cancer (*61*). Constitutive activation of cGAS in cancer cells results in continuous secretion of interferon-I (IFN-I), cytokines, and cGAMP into the extracellular space, attracting NK cells, DCs, macrophages, and $CD4^+$ and $CD8^+$ T cells to mount antitumor immunity (*40*, *41*, *62*). Nevertheless, it remains to be confirmed whether the increase in cytosolic levels of mtDNA was due to exogenous transfer or endogenous mtDNA leakage.

Finally, our results showed a decrease in osteocyte number and MFN2 levels, as well as intercellular mitochondrial transfer between osteocytes and cancer cells in aging mice. A recent study found that age-induced changes in the microenvironment promote the reactivation of dormant cancer cells (*63*). Aging leads to an imbalance in bone homeostasis, along with a decline in osteocyte density and proper functions, including mitochondrial transfer levels within the osteocyte dendritic network (*11*, *64*). We provided a possible perspective to understand how age-induced changes in the bone microenvironment may influence the biological behavior of cancer cells and further clinical outcomes of cancer patients. Future work will be needed to investigate if regulating osteocyte mitochondria may represent a therapeutic target for bone metastasis treatment.

MATERIALS AND METHODS

Cell lines

The murine osteocyte cell line MLO-Y4 was a gift from M. H. Zheng at Medical School, University of Western Australia. The murine breast cancer cell line E0771 (CRL-3461) was obtained from the American Type Culture Collection (ATCC). The murine Lewis lung cancer cell line LLC (TCM7), murine osteosarcoma cell line K7M2(TCM38), and human embryonic kidney cell line 293T (GNHu17) were obtained from the Cell Collection of the Chinese Academy of Science (Shanghai, China). MLO-Y4 cells were maintained in α-minimal essential medium (α-MEM; Gibco) with 10% fetal bovine serum (FBS; Gibco) and 1% penicillin/streptomycin (P/S) (Sigma-Aldrich). LLC, K7M2, E0771, and 293T cells were cultured in Dulbecco's modified Eagle's medium (DMEM; Gibco) with 10% FBS and 1% P/S. All cells were cultured in a 5% CO_2 atmosphere at 37°C. All cell lines were free of mycoplasma and underwent DNA STR (short tandem repeat) genotyping for cell identification.

Mice

PhAM^{floxed} mice [B6;129S-*Gt(ROSA)26Sor*$^{tm1(CAG-COX8A/Dendra2)Dcc}$/J, stock number 018385], *Mfn2*^{loxP} mice [B6.129(Cg)-*Mfn2*^{tm3Dcc}/J, stock number 026525], *Rhot1*^{loxP} mice [B6(Cg)-*Rhot1*$^{tm2.1Jmsu}$/J, stock number 031126], and B6-iDTR mice [C57BL/*6Gt(ROSA)26Sor*$^{tm1(HBEGF)Awai}$/J, stock number 007900] were purchased from the Jackson Laboratory. The 9.6-kb *Dmp1*^{Cre} transgenic mice [B6N.FVB-Tg(Dmp1-cre)1Jqfe/BwdJ, stock number 023047] were provided by J. Q. (Jerry) Feng at Texas A&M College of Dentistry, USA. B6-G/R mice [B6/JNju-*H11*$^{em1Cin(CAG-LoxP-ZsGreen-Stop-LoxP-tdTomato)}$/Nju, stock number T006163] were purchased from GemPharmatech Biological Technology Co. Ltd. All animals were maintained in a specific pathogen–free (SPF) facility with a temperature between 21 ± 2°C, humidity of 45 to 65%, and a regulated 12-hour light/dark cycle. The animals were provided with normal diet food and water ad libitum. All animal care and experimental protocols were designed and performed in compliance with the National Institutes of Health (NIH) *Guide for the Care and Use of Laboratory Animals* and the Guide of the Animal Care Committee of Zhejiang University.

Osteocyte ablation

Ten-week-old female Dmp1-cre iDTR$^{fl/fl}$ mice and iDTR$^{fl/fl}$ littermate controls were injected intraperitoneally with 25 ng of DT diluted in 1× phosphate-buffered saline (PBS) for two continuous days.

Tumor implantation

For intra-tibial injection model, a total of 1×10^6 LLC cells were resuspended in 10 μl of PBS and injected into the bone marrow cavity of the right tibia of each animal. After 2 weeks, the tumors were removed and weighed. Tumor volume was calculated using the formula $0.5 \times \text{length} \times \text{weight}^2$. For intra-iliac artery injection model, animals were anesthetized and restrained on a warming pad. A 7- to 8-mm incision was made between left hindlimb and abdomen to expose the common iliac vessels. LLC cells (1×10^4) were injected into the iliac artery to generate bone metastases. All experiments were designed and performed in compliance with the NIH *Guide for the Care and Use of Laboratory Animals* and the Guide of the Animal Care Committee of Zhejiang University. Cytokines and chemokines levels within cancer lesions were measured using a Mouse Cytokine Array/Chemokine Array ABplex (ABclonal Technology, Wuhan, China).

Bioluminescence imaging

In vivo bioluminescence imaging was performed weekly with IVIS Spectrum (PerkinElmer). Briefly, animals were anesthetized and imaged immediately after intraperitoneal injection of 100 μl of D-luciferin (15 mg/ml) (Invitrogen, catalog no. L2916). To quantify the metastatic burden, the total flux was calculated over the same region of interest using Living Image software (PerkinElmer).

Cell transfection

The mito-dendra2 plasmid was a gift from D. Chan (Addgene plasmid #55796) and cloned into the modified pHAGE vector containing Flag using restriction enzymes Not I and Bam HI. The double oligonucleotides were annealed at 95°C for 20 min and cloned into the pHAGE lentivirus vector. When 293T cells were at 70% confluency, they were cotransfected with a plasmid for mito-dendra2 and the lentivirus packaging plasmid (VSVG and Δ8.9) using Lipofectamine 3000 transfection reagents following the manufacturer's protocol. The lentiviral particles were harvested from the medium after 48 hours of cotransfection. The cell medium was passed through a 0.22-μm filter, and the lentivirus was collected into Eppendorf tubes and kept at −20°C for short-term storage or at −80°C for long-term storage.

The shRNA oligonucleotides for *Mfn2* or *Rhot1* were synthesized by Tsingke Biotechnology Co. Ltd. (Beijing, China); the detailed sequences are *Mfn2*#1 5′-GCTGGACAGCTGGATTGATAA-3′, *Mfn2*#2 5′-GGCAGTTTGAGGAGTGCATTT-3′, *Rhot1*#1 5′-GCTCAACTTCTTCCAGAGAAT-3′, and *Rhot1*#2 5′-GATATCTCAGAGTCGGAATTT-3′. The double oligonucleotides were annealed at 95°C for 20 min and cloned into the pLKO.1-hygro lentivirus vector. When 293T cells were at 70% confluency, they were cotransfected with plasmids and the lentivirus packaging plasmid (psPAX2 and pMD2.G) using Lipofectamine 3000 transfection reagents (Thermo Fisher Scientific, catalog no. L3000001) following the manufacturer's protocol. An appropriate empty vector was created for shRNA constructs. The lentiviral particles were harvested from the medium after 48 hours of cotransfection. The cell medium was passed through a 0.22-μm filter, and the lentivirus was collected into Eppendorf tubes and kept at −20°C for short-term storage or at −80°C for long-term storage.

LLC, K7M2, and E0771 cells were transfected with pLenti-CMV-mCherry-puro lentivirus (purchased from OBiO Technology Corp. Ltd.) with polybrene (10 μg/ml) (Sigma-Aldrich, catalog no. H9268) and selected by puromycin (3 μg/ml) (Gibco, catalog no. A1113802) to construct stable mCherry-expressing cell lines. MLO-Y4 cells were transfected with pHAGE-mito-dendra2 with polybrene (10 μg/ml) and selected by puromycin (10 μg/ml) for stable production of mitochondria-specific Dendra2-tagged protein (MLO-Y4-mtDendra2). For *Mfn2* or *Rhot1* KD, MLO-Y4-mtDendra2 cells were transfected with lentivirus-carrying pLKO.1-shMfn2#1, pLKO.1-shMfn2#2, pLKO.1-shRhot1#1, pLKO.1-shRhot1#2, and their empty control pLKO.1-shCtrl with polybrene (10 μg/ml) for 48 hours and selected by hygromycin (500 μg/ml) (Thermo Fisher Scientific, catalog no. 10687010). Stable cell lines were cultured in hygromycin (500 μg/ml). For *Cgas* or *Bax* KD, LLC or MLO-Y4 cells were transfected with *Cgas* small interfering RNA (siRNA), *Bax* siRNA, or negative control siRNA (Genomeditech Co. Ltd.) relatively using Lipofectamine 3000 transfection reagents. For *Mfn2* or *Rhot1* overexpression in MLO-Y4 cells, MLO-Y4-mtDendra2 cells were transfected with pLenti-CMV-Mfn2-BSR or pLenti-CMV-Rhot1-BSR (purchased from OBiO Technology Corp. Ltd.) with polybrene (10 μg/ml) for 48 hours and selected by blasticidin (10 μg/ml) (Thermo Fisher Scientific, catalog no. A1113902).

Mitochondrial isolation and artificial transfer

Mitochondria were isolated using a mitochondria isolation kit for cultured cells (Thermo Fisher Scientific, catalog no. 89874) following the manufacturer's instructions. The isolated mitochondria were resuspended in DMEM containing 5% FBS on ice and immediately used for artificial mitochondria transfer. LLC cancer cells were seeded in six-well plates (1×10^6 per well) the day before. The medium containing mitochondria was slowly added to the bottom of the well. The culture plate was centrifuged at 1000*g* for 10 min at 20°C. The plate was placed in a 37°C, 5% CO_2 incubator for 1 hour before a second centrifugation at 1000*g* for 10 min at 20°C.

Mitochondrial DNA isolation and transfection

mtDNA was isolated from MLO-Y4 cells using a mitochondria DNA isolation kit (BioVison, catalog no. K280-50) following the manufacturer's instructions. The mtDNA was dissolved in Tris-EDTA (TE) buffer and stored at −20°C. LLC cancer cells were seeded in six-well plates (1×10^6 per well) the day before and transfected with 5 mg of mtDNA per well using Lipofectamine 3000 (Thermo Fisher Scientific) according to the manufacturer's instructions.

Seahorse oxygen consumption

An XF96 extracellular flux analyzer (Agilent Technologies) was used to determine mitochondrial respiration levels using the Agilent Seahorse XF Cell Mito Stress Test Kit following the manufacturer's instructions. In brief, 1.0×10^4 treated LLC cells were seeded onto XF96 cell culture microplate per well. The oxygen consumption ratio (OCR) was assessed in glucose-containing XF base medium (25 mM glucose, 2 mM pyruvate glutamine, and 1 mM pyruvate) according to the manufacturer's instructions. The concentrations of oligomycin, carbonyl cyanide-4-(trifluoromethoxy) phenylhydrazone (FCCP), and antimycin A/rotenone were 1.5, 0.5, and 1.0 M, respectively.

Subcellular fractionation

LLC cancer cells seeded in a six-well plate were harvested with trypsin-EDTA, centrifuged at 500*g* for 5 min, and then washed with cold PBS. Cells were resuspended in 150 μl of digitonin lysis buffer (150 mM NaCl, 50 mM Hepes, pH 7.4, 25 μg/ml digitonin, protease, and phosphatase inhibitors) and incubated on ice for 10 min. Lysates were centrifuged at 2000*g* for 10 min at 4°C. Supernatants were transferred into a new 1.5-ml tube and centrifuged for 20 min at 20,000*g* at 4°C, and the supernatant was transferred again into a new prechilled tube. This process was repeated until the initial supernatant was centrifuged three times at 20,000*g*. The final supernatant was the clean cytosolic fraction. The cytosolic fraction was split into two fractions for DNA extraction and Western blotting. The initial pellet from the first centrifugation was washed with 1 ml of ice-cold PBS and centrifuged again for 5 min at 20,000*g*. The pellet was resuspended in 150 μl of NP-40 lysis buffer (150 mM NaCl, 50 mM Hepes, pH 7.4, 1% NP-40, protease, and phosphatase inhibitors) and incubated on ice for 30 min. The lysate was centrifuged at 7000*g* for 10 min at 4°C. The supernatant was the mitochondrial fraction stored for Western blotting analysis. The pellet fraction, which contains nuclei, was suspended and washed with 1 ml of ice-cold PBS. The resulting pellet was resuspended in 150 μl of radioimmunoprecipitation assay (RIPA) buffer (Sigma-Aldrich). The nuclear fraction was split again for DNA extraction and protein detection.

DNA extraction and mtDNA copy number analysis

Total DNA was extracted from the mitochondrial fraction or nuclear fraction using the FastPure Cell/Tissue Total RNA Isolation Kit (Vazyme, catalog no. RC112–01) following the manufacturer's instructions. One hundred nanograms of isolated DNA was analyzed by quantitative real-time PCR. mtDNA and nuclear DNA contents were determined by amplifying a short region of the mitochondrially encoded 16*S* rRNA, ND1, and 18*S* rRNA, and the mtDNA copy number was calculated as the mtDNA/nDNA ratio (*65*). Primer sequences are shown in table S2.

Flow cytometry and FACS

Tumor tissues were dissociated in DMEM with collagenase type IV (2 mg/ml, Sigma-Aldrich), deoxyribonuclease (0.1 mg/ml, Sigma-Aldrich), hyaluronidase (0.1 mg/ml, Sigma-Aldrich), and bovine serum albumin (BSA) (1 mg/ml, Sigma-Aldrich) at 37°C for 1 hour and then filtered through 70-μm filters (Falcon) to obtain single-cell suspensions. Cells were washed in PBS and blocked with TruStain FcX (anti-mouse CD16/32) antibody (BioLegend, catalog no. 101319) and incubated with Zombie Aqua Fixable Viability Kit (BioLegend, catalog no. 423107) or the Zombie UV Fixable Viability Kit (BioLegend, catalog no. 423101) for dead cell exclusion and with cell surface markers. For intracellular staining, cells were washed in PBS, fixed and permeabilized with the True-Nuclear Transcription Factor Buffer Set (BioLegend, catalog no. 424401) according to the manufacturer's instructions, and incubated with antibodies (listed below) for 20 min in the dark at room temperature. Flow cytometry analyses were performed using Beckman Coulter CytoFLEX LX and CytExpert v2.4 software, and data were analyzed using FlowJo v10. FACS was performed using Beckman MoFlo Astrios EQs and Summit v6.3.1 software. The single-cell suspensions were stained with the following antibodies: Brilliant Violet 605 anti-mouse CD45 (1:200, BioLegend, catalog no. 103139), Alexa Fluor 700 anti-mouse CD45 (1:200, BioLegend, catalog no. 147716), phycoerythrin (PE) anti-mouse F4/80 (1:200, BioLegend, catalog no. 157304), Brilliant Violet 785 anti-mouse CD11b (1:200, BioLegend, catalog no. 101243), PE/Dazzle 594 anti-mouse CD11c (1:200, BioLegend, catalog no. 117348), fluorescein isothiocyanate (FITC) anti-mouse I-A/I-E (1:200, BioLegend, catalog no. 107605), allophycocyanin (APC)/Fire 750 anti-mouse CD3 (1:200, BioLegend, catalog no. 100247), PE anti-mouse CD4 (1:200, BioLegend, catalog no. 100407), PE/Cyanine7 anti-mouse CD8a (1:200, BioLegend, catalog no. 100721), Alexa Fluor 647 anti-human/mouse granzyme B (1:200, BioLegend, catalog no. 515405), and FITC anti-mouse NK-1.1 (1:200, BioLegend, catalog no. 156507).

Single-cell RNA sequencing

Tumors were harvested from three mice in each group, dissociated, and sorted by FACS to obtain single-cell suspensions. The cells were loaded on a 10X Chromium Controller (10X Genomics) to generate nanoliter-scale gel beads-in-emulsions (GEMs). Barcoded scRNA-seq libraries were prepared using the Chromium Single Cell 3′ Reagent Kit. Then, the GEMs were used to generate barcoded, full-length cDNA through reverse transcription reactions. Next, the barcoded, full-length cDNA was used for library construction via fragmentation, end repair, A-tailing, ligation to an index adaptor, and amplification by PCR. The final libraries were sequenced on a HiSeq X Ten platform (Illumina), and 150 base pair (bp) paired-end reads were generated.

Raw data processing, quality control, and downstream analysis

Cell Ranger software (https://support.10xgenomics.com/single-cell-gene-expression/software/overview/welcome) was used to process the raw data and generate the UMI matrix. Cells with fewer than 500 unique molecular identifiers (UMIs) or with over 10% of transcripts derived from mitochondria were considered low-quality cells and were discarded. Downstream analyses were performed with Seurat (https://satijalab.org/seurat/). After principal components analysis (PCA), the top 10 PCs were used to perform t-SNE analysis.

Western blotting

Cells were lysed with RIPA buffer (Thermo Fisher Scientific, catalog no. 89901) with protease inhibitor (Thermo Fisher Scientific, catalog no. 78438) and phosphatase inhibitor (Thermo Fisher Scientific, catalog no. 78420). Cortical bone protein extraction was performed as described in our previous work (*11*). Protein concentrations were calculated using a BCA Protein Assay Kit (Thermo Fisher Scientific, catalog no. 23227). Protein extracts were diluted with 4× SDS sampling buffer and boiled for 5 min. Samples were separated by SDS–polyacrylamide gel electrophoresis (PAGE) and then electroblotted onto polyvinylidene difluoride membranes (Merck Millipore). After 1 hour of blocking with 5% milk in Tris-buffered saline with Tween 20 (TBST) buffer, membranes were incubated with primary antibodies at 4°C overnight. Membranes were washed with TBST buffer, incubated with corresponding horseradish peroxidase–conjugated secondary antibodies at room temperature for 1 hour, and washed with TBST buffer. Immunoreactive bands were detected using an Amersham ImageQuant 800 Western blot imaging system (ImageQuant 800 Control software v2.0.0). The following antibodies were used for immunoblotting: α-tubulin (1:1000, Cell Signaling Technology, catalog no. 3873), GAPDH (1:3000, Proteintech, catalog no. 10494-1-AP),

β-actin (1:3000, Proteintech, catalog no. 81115-1-RR), DMP1 (1:1000, Invitrogen, catalog no. PA5-88069), Rho T1 (1:1000, Santa Cruz Biotechnology, catalog no. sc-398520), MFN2 (1:1000, Cell Signaling Technology, catalog no. 9482), Tom20 (1:1000, Cell Signaling Technology, catalog no. 42406), lamin A/C (1:1000, Cell Signaling Technology, catalog no. 4777), anti-VDAC1/Porin + VDAC2 (1:1000, Abcam, catalog no. ab154856), STING (1:1000, Cell Signaling Technology, catalog no. 50494), phospho-STING (1:1000, Cell Signaling Technology, catalog no. 72971), cGAS (1:1000, Cell Signaling Technology, catalog no. 31659), TBK1/NAK (1:1000, Cell Signaling Technology, catalog no. 3504), phospho-TB1/NAK (1:1000, Cell Signaling Technology, catalog no. 5483), IRF3 (1:1000, Cell Signaling Technology, catalog no. 4302), phospho-IRF3 (1:1000, Cell Signaling Technology, catalog no. 29047), NF-κB p65 (1:1000, Cell Signaling Technology, catalog no. 8242), and phospho–NF-κB p65 (1:1000, Cell Signaling Technology, catalog no. 3033).

Histopathology

Mouse femurs and tibias were dissected and fixed in 4% PFA at 4°C for 24 hours and decalcified in 10% EDTA (pH 7.2) at 4°C for 2 weeks (renewed every other day). Bones were processed, embedded in paraffin, and sectioned at 6 μm thickness. Hematoxylin and eosin staining was performed, and slides were scanned using a Leica DM2 B microscope (Leica) and LAS X software (Leica). ImageJ was used to measure osteocyte number and empty lacunae.

Whole-mount staining

Tumor-bearing tibias were dissected and fixed in 4% paraformaldehyde (PFA) at 4°C overnight. Then, the tissues were cryopreserved in 30% sucrose-PBS and embedded in optimal cutting temperature (OCT) compound. OCT-embedded tibias were shaved at 20-μm intervals parallel to the long axis of the tibia until the maximum cross section of the tibia was observed on a Thermo Cryotome FSE (Thermo Fisher Scientific). The remaining OCT was melted at room temperature and washed three times in PBS for 10 min. Then, the samples were blocked overnight in 3% BSA and 5% goat serum plus 0.05% Triton X-100 in PBS. Following blocking/permeabilization, tibias were incubated for 24 hours at 4°C with 1% Alexa Fluor 680 Phalloidin (Invitrogen, catalog no. A22286) in the dark. The samples were washed three times with PBS for 10 min and then stained with 4′,6-diamidino-2-phenylindole (DAPI) (1:1000, Roche, catalog no. 10236276001) for 1 hour. Tibias were washed again and inverted in ProLong Diamond antifade reagent (Invitrogen, catalog no. P36970) in a confocal dish (MatTek, P35G-1.5-20-C). Images were obtained using Leica software on a Leica confocal microscope platform STELLARIS 5 (Leica).

Immunofluorescence

Cells seeded in the confocal dish were washed with PBS, fixed in 4% PFA for 15 min at room temperature, and blocked/permeabilized in 3% BSA, 5% goat serum, and 0.05% Triton X-100 in PBS for 1 hour at room temperature. Cells were incubated in 5% BSA in PBS containing antibodies overnight at 4°C. Cells were washed three times with PBS and incubated with corresponding secondary antibodies (1:1000, Invitrogen) for 2 hours at room temperature in the dark. Cells were incubated with DAPI (1:5000) for 15 min for nuclear staining. Cells were washed three more times with PBS and mounted in ProLong Diamond antifade reagent. Images were obtained using LAS X software (Leica) on a Leica confocal microscope platform STELLARIS 5. The following antibodies were used for immunostaining: α-tubulin (1:1000, Cell Signaling Technology, catalog no. 3873), Tom20 (1:100, Cell Signaling Technology, catalog no. 42406), and dsDNA (1:200, Sigma-Aldrich, catalog no. CBL186).

Cell imaging and analysis

Fixed cells and tissue images were acquired on a Leica confocal microscope platform STELLARIS 5 using a 63× oil immersion objective. Live-cell images were acquired on a Leica confocal microscope platform STELLARIS 5 using incubation systems at 37°C with 5% CO_2. Postprocessing of the images was performed using ImageJ or LAS X software (Leica).

Micro-CT analysis

Tibias were harvested for micro-CT imaging. Micro-CT was performed using a Skyscan 1276 instrument (Bruker-MicroCT, Kontich, Belgium) with a resolution of 10 μm using manufacturer-provided software. Micro-CT images were reconstructed using CTvox software v3.3 and analyzed using CTan software v1.07.

RNA extraction and real-time PCR

Total RNA was isolated using RNAiso reagent (TaKaRa). Reverse transcription was achieved using a cDNA Synthesis Kit (TaKaRa). Real-time quantitative PCR was performed using SYBR Premix Ex Taq kits (TaKaRa) in an Applied Biosystems 7500 system. Each sample was run in triplicate, and gene expression levels were normalized to β-actin levels. The primer sequences are listed in table S2.

Statistical analysis

Statistical analysis was performed using GraphPad Prism 8.0 (GraphPad Software, San Diego, CA) statistical software. Values of $P < 0.05$ were considered statistically significant. Data are presented as means ± SEM. Unpaired or paired two-tailed Student's t tests were used to compare differences between two independent groups. One-way analysis of variance (ANOVA) followed by Tukey's multiple comparisons test was used to compare differences among multiple groups.

Supplementary Materials

This PDF file includes:

Figs. S1 to S8
Tables S1 and S2

REFERENCES AND NOTES

1. K. Ganesh, J. Massague, Targeting metastatic cancer. *Nat. Med.* **27**, 34–44 (2021).
2. R. E. Coleman, P. I. Croucher, A. R. Padhani, P. Clézardin, E. Chow, M. Fallon, T. Guise, S. Colangeli, R. Capanna, L. Costa, Bone metastases. *Nat. Rev. Dis. Primers* **6**, 83 (2020).
3. J. Fornetti, A. L. Welm, S. A. Stewart, Understanding the bone in cancer metastasis. *J. Bone Miner. Res.* **33**, 2099–2113 (2018).
4. L. C. Hofbauer, A. Bozec, M. Rauner, F. Jakob, S. Perner, K. Pantel, Novel approaches to target the microenvironment of bone metastasis. *Nat. Rev. Clin.* **18**, 488–505 (2021).
5. L. F. Bonewald, The amazing osteocyte. *J. Bone Miner.* **26**, 229–238 (2011).
6. J. Delgado-Calle, T. Bellido, The osteocyte as a signaling cell. *Physiol. Rev.* **102**, 379–410 (2022).
7. J. L. Sottnik, J. Dai, H. Zhang, B. Campbell, E. T. Keller, Tumor-induced pressure in the bone microenvironment causes osteocytes to promote the growth of prostate cancer bone metastases. *Cancer Res.* **75**, 2151–2158 (2015).
8. J. Z. Zhou, M. A. Riquelme, S. Gu, R. Kar, X. Gao, L. Sun, J. X. Jiang, Osteocytic connexin hemichannels suppress breast cancer growth and bone metastasis. *Oncogene* **35**, 5597–5607 (2016).

9. S. Liu, D. Wu, X. Sun, Y. Fan, R. Zha, A. Jalali, Y. Feng, K. Li, T. Sano, N. Vike, F. Li, J. Rispoli, A. Sudo, J. Liu, A. Robling, H. Nakshatri, B. Y. Li, H. Yokota, Overexpression of Lrp5 enhanced the anti-breast cancer effects of osteocytes in bone. *Bone Res.* **9**, 32 (2021).
10. H. Hemmatian, S. Conrad, G. Furesi, K. Mletzko, J. Krug, A. V. Faila, J. D. Kuhlmann, M. Rauner, B. Busse, K. Jähn-Rickert, Reorganization of the osteocyte lacuno-canalicular network characteristics in tumor sites of an immunocompetent murine model of osteotropic cancers. *Bone* **152**, 116074 (2021).
11. J. Gao, A. Qin, D. Liu, R. Ruan, Q. Wang, J. Yuan, T. S. Cheng, A. Filipovska, J. M. Papadimitriou, K. Dai, Q. Jiang, X. Gao, J. Q. Feng, H. Takayanagi, C. Zhang, M. H. Zheng, Endoplasmic reticulum mediates mitochondrial transfer within the osteocyte dendritic network. *Sci. Adv.* **5**, eaaw7215 (2019).
12. N. S. Chandel, Evolution of mitochondria as signaling organelles. *Cell Metab.* **22**, 204–206 (2015).
13. M. Picard, O. S. Shirihai, Mitochondrial signal transduction. *Cell Metab.* **34**, 1620–1653 (2022).
14. L. F. Dong, J. Rohlena, R. Zobalova, Z. Nahacka, A. M. Rodriguez, M. V. Berridge, J. Neuzil, Mitochondria on the move: Horizontal mitochondrial transfer in disease and health. *J. Cell Biol.* **222**, e202211044 (2023).
15. J. Levoux, A. Prola, P. Lafuste, M. Gervais, N. Chevallier, Z. Koumaiha, K. Kefi, L. Braud, A. Schmitt, A. Yacia, A. Schirmann, B. Hersant, M. Sid-Ahmed, S. B. Larbi, K. Komrskova, J. Rohlena, F. Relaix, J. Neuzil, A.-M. Rodriguez, Platelets facilitate the wound-healing capability of mesenchymal stem cells by mitochondrial transfer and metabolic reprogramming. *Cell Metab.* **33**, 283–299.e289 (2021).
16. C. R. Marlein, R. E. Piddock, J. J. Mistry, L. Zaitseva, C. Hellmich, R. H. Horton, Z. Zhou, M. J. Auger, K. M. Bowles, S. A. Rushworth, CD38-driven mitochondrial trafficking promotes bioenergetic plasticity in multiple myeloma. *Cancer Res.* **79**, 2285–2297 (2019).
17. K. Piekarska, Z. Urban-Wójciuk, M. Kurkowiak, I. Pelikant-Małecka, A. Schumacher, J. Sakowska, J. H. Spodnik, Ł. Arcimowicz, H. Zielińska, B. Tymoniuk, A. Renkielska, J. Siebert, E. Słomińska, P. Trzonkowski, T. Hupp, N. M. Marek-Trzonkowska, Mesenchymal stem cells transfer mitochondria to allogeneic Tregs in an HLA-dependent manner improving their immunosuppressive activity. *Nat. Commun.* **13**, 856 (2022).
18. T. Saha, C. Dash, R. Jayabalan, S. Khiste, A. Kulkarni, K. Kurmi, J. Mondal, P. K. Majumder, A. Bardia, H. L. Jang, S. Sengupta, Intercellular nanotubes mediate mitochondrial trafficking between cancer and immune cells. *Nat. Nanotechnol.* **17**, 98–106 (2022).
19. T. Buch, F. L. Heppner, C. Tertilt, T. J. A. J. Heinen, M. Kremer, F. T. Wunderlich, S. Jung, A. Waisman, A Cre-inducible diphtheria toxin receptor mediates cell lineage ablation after toxin administration. *Nat. Methods* **2**, 419–426 (2005).
20. Y. Lu, Y. Xie, S. Zhang, V. Dusevich, L. F. Bonewald, J. Q. Feng, DMP1-targeted Cre expression in odontoblasts and osteocytes. *J. Dent. Res.* **86**, 320–325 (2007).
21. S. Tatsumi, K. Ishii, N. Amizuka, M. Li, T. Kobayashi, K. Kohno, M. Ito, S. Takeshita, K. Ikeda, Targeted ablation of osteocytes induces osteoporosis with defective mechanotransduction. *Cell Metab.* **5**, 464–475 (2007).
22. M. D. Muzumdar, B. Tasic, K. Miyamichi, L. Li, L. Luo, A global double-fluorescent Cre reporter mouse. *Genesis* **45**, 593–605 (2007).
23. J. Q. Fen, J. Zhang, S. L. Dallas, Y. Lu, S. Chen, X. Tan, M. Owen, S. E. Harris, M. MacDougall, Dentin matrix protein 1, a target molecule for Cbfa1 in bone, is a unique bone marker gene. *J Bone Miner Res.* **17**, 1822–1831 (2002).
24. S. E. Youlten, J. P. Kemp, J. G. Logan, E. J. Ghirardello, C. M. Sergio, M. R. G. Dack, S. E. Guilfoyle, V. D. Leitch, N. C. Butterfield, D. Komla-Ebri, R. C. Chai, A. P. Corr, J. T. Smith, S. T. Mohanty, J. A. Morris, M. M. McDonald, J. M. W. Quinn, A. R. McGlade, N. Bartonicek, M. Jansson, K. Hatzikotoulas, M. D. Irving, A. Beleza-Meireles, F. Rivadeneira, E. Duncan, J. B. Richards, D. J. Adams, C. J. Lelliott, R. Brink, T. G. Phan, J. A. Eisman, D. M. Evans, E. Zeggini, P. A. Baldock, J. H. D. Bassett, G. R. Williams, P. I. Croucher, Osteocyte transcriptome mapping identifies a molecular landscape controlling skeletal homeostasis and susceptibility to skeletal disease. *Nat. Commun.* **12**, 2444 (2021).
25. A. H. Pham, J. M. McCaffery, D. C. Chan, Mouse lines with photo-activatable mitochondria to study mitochondrial dynamics. *Genesis* **50**, 833–843 (2012).
26. H. Scheiblich, C. Dansokho, D. Mercan, S. V. Schmidt, L. Bousset, L. Wischhof, F. Eikens, A. Odainic, J. Spitzer, A. Griep, S. Schwartz, D. Bano, E. Latz, R. Melki, M. T. Heneka, Microglia jointly degrade fibrillar alpha-synuclein cargo by distribution through tunneling nanotubes. *Cell* **184**, 5089–5106.e5021 (2021).
27. M. N. Islam, S. R. das, M. T. Emin, M. Wei, L. Sun, K. Westphalen, D. J. Rowlands, S. K. Quadri, S. Bhattacharya, J. Bhattacharya, Mitochondrial transfer from bone-marrow-derived stromal cells to pulmonary alveoli protects against acute lung injury. *Nat. Med.* **18**, 759–765 (2012).
28. R. P. Norris, Transfer of mitochondria and endosomes between cells by gap junction internalization. *Traffic* **22**, 174–179 (2021).
29. M. Rosina, V. Ceci, R. Turchi, L. Chuan, N. Borcherding, F. Sciarretta, M. Sánchez-Díaz, F. Tortolici, K. Karlinsey, V. Chiurchiù, C. Fuoco, R. Giwa, R. L. Field, M. Audano, S. Arena, A. Palma, F. Riccio, F. Shamsi, G. Renzone, M. Verri, A. Crescenzi, S. Rizza, F. Faienza, G. Filomeni, S. Kooijman, S. Rufini, A. A. F. de Vries, A. Scaloni, N. Mitro, Y.-H. Tseng, A. Hidalgo, B. Zhou, J. R. Brestoff, K. Aquilano, D. Lettieri-Barbato, Ejection of damaged mitochondria and their removal by macrophages ensure efficient thermogenesis in brown adipose tissue. *Cell Metab.* **34**, 533–548.e512 (2022).
30. J. R. Brestoff, C. B. Wilen, J. R. Moley, Y. Li, W. Zou, N. P. Malvin, M. N. Rowen, B. T. Saunders, H. Ma, M. R. Mack, B. L. Hykes Jr., D. R. Balce, A. Orvedahl, J. W. Williams, N. Rohatgi, X. Wang, M. R. Mc Allaster, S. A. Handley, B. S. Kim, J. G. Doench, B. H. Zinselmeyer, M. S. Diamond, H. W. Virgin, A. E. Gelman, S. L. Teitelbaum, Intercellular mitochondria transfer to macrophages regulates white adipose tissue homeostasis and is impaired in obesity. *Cell Metab.* **33**, 270–282 (2021).
31. K. Brickley, F. A. Stephenson, Trafficking kinesin protein (TRAK)-mediated transport of mitochondria in axons of hippocampal neurons. *J. Biol. Chem.* **286**, 18079–18092 (2011).
32. K. T. Chang, R. F. Niescier, K.-T. Min, Mitochondrial matrix Ca2+ as an intrinsic signal regulating mitochondrial motility in axons. *Proc. Natl. Acad. Sci. U.S.A.* **108**, 15456–15461 (2011).
33. H. Chen, J. M. McCaffery, D. C. Chan, Mitochondrial fusion protects against neurodegeneration in the cerebellum. *Cell* **130**, 548–562 (2007).
34. A. S. Tan, J. W. Baty, L. F. Dong, A. Bezawork-Geleta, B. Endaya, J. Goodwin, M. Bajzikova, J. Kovarova, M. Peterka, B. Yan, E. A. Pesdar, M. Sobol, A. Filimonenko, S. Stuart, M. Vondrusova, K. Kluckova, K. Sachaphibulkij, J. Rohlena, P. Hozak, J. Truksa, D. Eccles, L. M. Haupt, L. R. Griffiths, J. Neuzil, M. V. Berridge, Mitochondrial genome acquisition restores respiratory function and tumorigenic potential of cancer cells without mitochondrial DNA. *Cell Metab.* **21**, 81–94 (2015).
35. M. Bajzikova, J. Kovarova, A. R. Coelho, S. Boukalova, S. Oh, K. Rohlenova, D. Svec, S. Hubackova, B. Endaya, K. Judasova, A. Bezawork-Geleta, K. Kluckova, L. Chatre, R. Zobalova, A. Novakova, K. Vanova, Z. Ezrova, G. J. Maghzal, S. M. Novais, M. Olsinova, L. Krobova, Y. J. An, E. Davidova, Z. Nahacka, M. Sobol, T. Cunha-Oliveira, C. Sandoval-Acuña, H. Strnad, T. Zhang, T. Huynh, T. L. Serafim, P. Hozak, V. A. Sardao, W. J. H. Koopman, M. Ricchetti, P. J. Oliveira, F. Kolar, M. Kubista, J. Truksa, K. Dvorakova-Hortova, K. Pacak, R. Gurlich, R. Stocker, Y. Zhou, M. V. Berridge, S. Park, L. Dong, J. Rohlena, J. Neuzil, Reactivation of dihydroorotate dehydrogenase-driven pyrimidine biosynthesis restores tumor growth of respiration-deficient cancer cells. *Cell Metab.* **29**, 399–416.e310 (2019).
36. N. Samson, A. Ablasser, The cGAS-STING pathway and cancer. *Nat. Cancer* **3**, 1452–1463 (2022).
37. A. Caicedo, V. Fritz, J. M. Brondello, M. Ayala, I. Dennemont, N. Abdellaoui, F. de Fraipont, A. Moisan, C. A. Prouteau, H. Boukhaddaoui, C. Jorgensen, M. L. Vignais, MitoCeption as a new tool to assess the effects of mesenchymal stem/stromal cell mitochondria on cancer cell metabolism and function. *Sci. Rep.* **5**, 9073 (2015).
38. K. McArthur, L. W. Whitehead, J. M. Heddleston, L. Li, B. S. Padman, V. Oorschot, N. D. Geoghegan, S. Chappaz, S. Davidson, H. San Chin, R. M. Lane, M. Dramicanin, T. L. Saunders, C. Sugiana, R. Lessene, L. D. Osellame, T. L. Chew, G. Dewson, M. Lazarou, G. Ramm, G. Lessene, M. T. Ryan, K. L. Rogers, M. F. van Delft, B. T. Kile, BAK/BAX macropores facilitate mitochondrial herniation and mtDNA efflux during apoptosis. *Science* **359**, eaao6047 (2018).
39. K. Cosentino, V. Hertlein, A. Jenner, T. Dellmann, M. Gojkovic, A. Peña-Blanco, S. Dadsena, N. Wajngarten, J. S. H. Danial, J. V. Thevathasan, M. Mund, J. Ries, A. J. Garcia-Saez, The interplay between BAX and BAK tunes apoptotic pore growth to control mitochondrial-DNA-mediated inflammation. *Mol. Cell* **82**, 933–949.e939 (2022).
40. A. Marcus, Tumor-derived cGAMP triggers a STING-mediated interferon response in non-tumor cells to activate the NK cell response. *Immunity* **49**, 754–763.e754 (2018).
41. L. Schadt, C. Sparano, N. A. Schweiger, K. Silina, V. Cecconi, G. Lucchiari, H. Yagita, E. Guggisberg, S. Saba, Z. Nascakova, W. Barchet, M. van den Broek, Cancer-cell-intrinsic cGAS expression mediates tumor immunogenicity. *Cell Rep.* **29**, 1236–1248.e1237 (2019).
42. S. K. Wculek, F. J. Cueto, A. M. Mujal, I. Melero, M. F. Krummel, D. Sancho, Dendritic cells in cancer immunology and immunotherapy. *Nat. Rev. Immunol.* **20**, 7–24 (2020).
43. J. Z. Zhou, M. A. Riquelme, X. Gao, L. G. Ellies, L. Z. Sun, J. X. Jiang, Differential impact of adenosine nucleotides released by osteocytes on breast cancer growth and bone metastasis. *Oncogene* **34**, 1831–1842 (2015).
44. J. Delgado-Calle, J. Anderson, M. D. Cregor, M. Hiasa, J. M. Chirgwin, N. Carlesso, T. Yoneda, K. S. Mohammad, L. I. Plotkin, G. D. Roodman, T. Bellido, Bidirectional notch signaling and osteocyte-derived factors in the bone marrow microenvironment promote tumor cell proliferation and bone destruction in multiple myeloma. *Cancer Res.* **76**, 1089–1100 (2016).
45. D. Liu, Y. Gao, J. Liu, Y. Huang, J. Yin, Y. Feng, L. Shi, B. P. Meloni, C. Zhang, M. Zheng, J. Gao, Intercellular mitochondrial transfer as a means of tissue revitalization. *Signal Transduct. Target. Ther.* **6**, 65 (2021).
46. K. Shen, C. L. Pender, R. Bar-Ziv, H. Zhang, K. Wickham, E. Willey, J. Durieux, Q. Ahmad, A. Dillin, Mitochondria as cellular and organismal signaling hubs. *Annu. Rev. Cell Dev. Biol.* **38**, 179–218 (2022).
47. A. G. Robling, L. F. Bonewald, The osteocyte: New insights. *Annu. Rev. Physiol.* **82**, 485–506 (2020).
48. P. Ding, C. Gao, Y. Gao, D. Liu, H. Li, J. Xu, X. Chen, Y. Huang, C. Zhang, M. Zheng, J. Gao, Osteocytes regulate senescence of bone and bone marrow. *eLife* **11**, e81480 (2022).

49. R. L. Siegel, K. D. Miller, H. E. Fuchs, A. Jemal, Cancer statistics, 2022. *CA Cancer J. Clin.* **72**, 7–33 (2022).
50. H. Sung, J. Ferlay, R. L. Siegel, M. Laversanne, I. Soerjomataram, A. Jemal, F. Bray, Global Cancer Statistics 2020: GLOBOCAN estimates of incidence and mortality worldwide for 36 cancers in 185 countries. *CA Cancer J. Clin.* **71**, 209–249 (2021).
51. P. R. Kumar, M. Saad, C. Hellmich, J. J. Mistry, J. A. Moore, S. Conway, C. J. Morris, K. M. Bowles, M. D. Moncrieff, S. A. Rushworth, PGC-1α induced mitochondrial biogenesis in stromal cells underpins mitochondrial transfer to melanoma. *Br. J. Cancer* **127**, 69–78 (2022).
52. L. F. Dong, J. Kovarova, M. Bajzikova, A. Bezawork-Geleta, D. Svec, B. Endaya, K. Sachaphibulkij, A. R. Coelho, N. Sebkova, A. Ruzickova, A. S. Tan, K. Kluckova, K. Judasova, K. Zamecnikova, Z. Rychtarcikova, V. Gopalan, L. Andera, M. Sobol, B. Yan, B. Pattnaik, N. Bhatraju, J. Truksa, P. Stopka, P. Hozak, A. K. Lam, R. Sedlacek, P. J. Oliveira, M. Kubista, A. Agrawal, K. Dvorakova-Hortova, J. Rohlena, M. V. Berridge, J. Neuzil, Horizontal transfer of whole mitochondria restores tumorigenic potential in mitochondrial DNA-deficient cancer cells. *eLife* **6**, e22187 (2017).
53. T. Ahmad, S. Mukherjee, B. Pattnaik, M. Kumar, S. Singh, M. Kumar, R. Rehman, B. K. Tiwari, K. A. Jha, A. P. Barhanpurkar, M. R. Wani, S. S. Roy, U. Mabalirajan, B. Ghosh, A. Agrawal, Miro1 regulates intercellular mitochondrial transport & enhances mesenchymal stem cell rescue efficacy. *EMBO J.* **33**, 994–1010 (2014).
54. C. A. Lee, L. S. Chin, L. Li, Hypertonia-linked protein Trak1 functions with mitofusins to promote mitochondrial tethering and fusion. *Protein Cell* **9**, 693–716 (2018).
55. A. Misko, S. Jiang, I. Wegorzewska, J. Milbrandt, R. H. Baloh, Mitofusin 2 is necessary for transport of axonal mitochondria and interacts with the Miro/Milton complex. *J. Neurosci.* **30**, 4232–4240 (2010).
56. C. R. Marlein, L. Zaitseva, R. E. Piddock, S. D. Robinson, D. R. Edwards, M. S. Shafat, Z. Zhou, M. Lawes, K. M. Bowles, S. A. Rushworth, NADPH oxidase-2 derived superoxide drives mitochondrial transfer from bone marrow stromal cells to leukemic blasts. *Blood* **130**, 1649–1660 (2017).
57. A. P. West, G. S. Shadel, Mitochondrial DNA in innate immune responses and inflammatory pathology. *Nat. Rev. Immunol.* **17**, 363–375 (2017).
58. D. Torralba, F. Baixauli, C. Villarroya-Beltri, I. Fernández-Delgado, A. Latorre-Pellicer, R. Acín-Pérez, N. B. Martín-Cófreces, Á. L. Jaso-Tamame, S. Iborra, I. Jorge, G. González-Aseguinolaza, J. Garaude, M. Vicente-Manzanares, J. A. Enríquez, M. Mittelbrunn, F. Sánchez-Madrid, Priming of dendritic cells by DNA-containing extracellular vesicles from activated T cells through antigen-driven contacts. *Nat. Commun.* **9**, 2658 (2018).
59. N. Rabas, S. Palmer, L. Mitchell, S. Ismail, A. Gohlke, J. S. Riley, S. W. G. Tait, P. Gammage, L. L. Soares, I. R. Macpherson, J. C. Norman, PINK1 drives production of mtDNA-containing extracellular vesicles to promote invasiveness. *J. Cell Biol.* **220**, e202006049 (2021).
60. H. W. S. Tan, G. Lu, H. Dong, Y. L. Cho, A. Natalia, L. Wang, C. Chan, D. Kappei, R. Taneja, S. C. Ling, H. Shao, S. Y. Tsai, W. X. Ding, H. M. Shen, A degradative to secretory autophagy switch mediates mitochondria clearance in the absence of the mATG8-conjugation machinery. *Nat. Commun.* **13**, 3720 (2022).
61. J. Kwon, S. F. Bakhoum, The cytosolic DNA-sensing cGAS-STING pathway in cancer. *Cancer Discov.* **10**, 26–39 (2020).
62. C. Chen, P. Xu, Cellular functions of cGAS-STING signaling. *Trends Cell Biol.* **33**, 630–648 (2022).
63. M. E. Fane, Y. Chhabra, G. M. Alicea, D. A. Maranto, S. M. Douglass, M. R. Webster, V. W. Rebecca, G. E. Marino, F. Almeida, B. L. Ecker, D. J. Zabransky, L. Hüser, T. Beer, H. Y. Tang, A. Kossenkov, M. Herlyn, D. W. Speicher, W. Xu, X. Xu, E. M. Jaffee, J. A. Aguirre-Ghiso, A. T. Weeraratna, Stromal changes in the aged lung induce an emergence from melanoma dormancy. *Nature* **606**, 396–405 (2022).
64. B. Busse, D. Djonic, P. Milovanovic, M. Hahn, K. Püschel, R. O. Ritchie, M. Djuric, M. Amling, Decrease in the osteocyte lacunar density accompanied by hypermineralized lacunar occlusion reveals failure and delay of remodeling in aged human bone. *Aging Cell* **9**, 1065–1075 (2010).
65. P. M. Quiros, A. Goyal, P. Jha, J. Auwerx, Analysis of mtDNA/nDNA ratio in mice. *Curr. Protoc. Mouse Biol.* **7**, 47–54 (2017).

Acknowledgments

Funding: This work was supported by the National Natural Science Foundation of China (82273178, 82072959, and 82002339); the Natural Science Foundation of Zhejiang Province, China (LD21H160002 and LQ22H160048); the Shanghai Frontiers Science Center of Degeneration and Regeneration in Skeletal System (BJ1-9000-22-4002); and the Medical and Health Science and Technology Plan of Department of Health of Zhejiang Province (2023558928). **Author contributions:** Z.Y., C.Z., and J.G. conceived, designed, and supervised the study. H.Z., W.Z., H.L., and F.X. designed the methods. H.Z., W.Z., F.X., E.Y., Y.X., T.C., S.W., Z.W., H.S., F.W., M.Y., H.M., and J.Z. performed the experiments. H.Z., W.Z., F.X., and B.L. contributed to the analysis of results. H.Z., Y.X., and X.C. performed bioinformatic analysis. M.D.D. proofread the manuscript. H.Z. wrote the original draft. Z.Y. and J.G. revised and edited the manuscript. Z.Y. is the lead contact. All authors contributed to and approved the final version of the manuscript. **Competing interests:** The authors declare that they have no competing interests. **Data and materials availability:** All data needed to evaluate the conclusions in the paper are present in the paper and/or the Supplementary Materials. The raw single-cell RNA-sequencing data of mice in different experiments (tumor-infiltrating cells in CAG-ZsGreen mice, osteocyte mitochondria recipient cells in DMP1-Cre PhAM mice, and tumor cells in $Dmp1^{Cre}$ $Mfn2^{-/-}$, $Dmp1^{Cre}$ $Rhot1^{-/-}$, and wild-type mice) generated in our study are deposited in the Gene Expression Omnibus (GEO) database under accession numbers GSE228609, GSE228613, and GSE228708, respectively. The raw RNA-sequencing data of cortical bones from young and aged mice generated in our study are deposited in the GEO database under accession number GSE235103. Source data are provided in this paper. The remaining data are provided in this article and the Supplementary Materials.

Submitted 26 April 2023
Accepted 18 December 2023
Published 17 January 2024
10.1126/sciadv.adi4298